

Fragmented atomic shell around S187 H II region and its interaction with molecular and ionized gas

Petr Zemlyanukha¹, Igor I. Zinchenko¹, Evgeny Dombek^{1,2}, Lev E. Pirogov¹, Anastasiia Topchieva³, Gilles Joncas⁴, Lokesh K. Dewangan⁵, Devendra K. Ojha⁶ and Swarna K. Ghosh⁶

¹*Institute of Applied Physics of the Russian Academy of Sciences, 46 Ul'yanov str., Nizhny Novgorod 603950, Russia*

²*Lobachevsky State University of Nizhny Novgorod, 23 Gagarin Ave, Nizhny Novgorod 603950, Russia*

³*Institute of Astronomy, Russian Academy of Sciences, Pyatnitskaya str., 48, Moscow, Russia*

⁴*Centre de Recherche en Astrophysique du Québec, Département de Physique, de génie physique et d'optique, Université Laval, Québec, QC, G1V 0A6, Canada*

⁵*Physical Research Laboratory, Navrangpura, Ahmedabad 380009, India*

⁶*Department of Astronomy and Astrophysics, Tata Institute of Fundamental Research, Homi Bhabha Road, Mumbai 400 005, India*

Accepted XXX. Received YYY; in original form ZZZ

ABSTRACT

The environment of S187, a nearby H II region (1.4 ± 0.3 kpc), is analyzed. A surrounding shell has been studied in the H I line, molecular lines, and also in infrared and radio continua. We report the first evidence of a clumpy HI environment in its photodissociation region. A background radio galaxy enables the estimation of the properties of cold atomic gas. The estimated atomic mass fraction of the shell is $\sim 260 M_{\odot}$, the median spin temperature is ~ 50 K, the shell size is ~ 4 pc with typical wall width around 0.2 pc. The atomic shell consists of ~ 100 fragments. The fragment sizes correlate with mass with a power-law index of 2.39–2.50. The S187 shell has a complex kinematical structure, including the expanding quasi spherical layer, molecular envelope, an atomic sub-bubble inside the shell and two dense cores (S187 SE and S187 NE) at different stages of evolution. The atomic sub-bubble inside the shell is young, contains a Class II young stellar object and OH maser in the centre and the associated YSOs in the walls of the bubble. S187 SE and S187 NE have similar masses ($\sim 1200 M_{\odot}$ and $\sim 900 M_{\odot}$, respectively). S187 SE is embedded into the atomic shell and has a number of associated objects including high mass protostars, outflows, maser sources and other indicators of ongoing star formation. No YSOs inside S187 NE were detected, but indications of compression and heating by the H II region exist.

Key words: stars: formation – ISM: clouds – radio lines:ISM - ISM: HII regions - ISM: evolution - ISM: bubbles

1 INTRODUCTION

The expansion of an H II region is thought to be a factor that induces star formation in the interstellar medium especially as a trigger of high mass star formation. Such a trigger can arise from the over-pressurization of gas that bounds the region (Thompson et al. 2004) leading to compression and fragmentation. The dynamics of this process is usually studied with C I/C II/O I observations (Requena-Torres et al. 2016; Okada et al. 2019; Bally et al. 2018). The atomic hydrogen production in a photodissociation region (PDR) is quite natural and is predicted by the existing models (Kirsanova & Wiebe 2019; Kirsanova et al. 2020; Sternberg et al. 2014). Still, there are few observations of atomic shells around H II regions in the neutral hydrogen line (Roger et al. 2004; Cichowolski et al. 2009; Joncas et al. 1992). Such rarity is caused by the challenges of H I observations. The H I emitting zone near the ionized region is usually garbled by the Galactic atomic gas in the line of sight. An estimation of the properties of the atomic gas is difficult. The H I spin temperature is correlated with the optical depth leading to uncertainties in estimations (Saha et al. 2018). Absorption profiles are essential for these estimations. Sometimes one is helped when a strong background

continuum source occurs behind the studied object (Nguyen et al. 2019).

To study the atomic hydrogen gas around a H II region, high resolution H I data should be obtained and compared with kinematics, morphology and properties of other species.

This paper presents such analysis for the S187 (Sh2-187, KR120, LBN 126.7-00.80) environment. This region is well-studied from the optical to the radio wavelengths. The S187 H II region (Fig. 1) is driven by a cluster of B0V stars with a photon flux of 10^{47} ionising photons s^{-1} (Joncas et al. 1992) historically named as S187 B or BD52. The region is fairly young with an estimated age of $\approx 5 \times 10^5$ yr (Joncas et al. 1992). The distance estimate is 1.4 ± 0.26 kpc from photometry (Russeil et al. 2007) and ~ 0.9 kpc from Gaia DR2 data and CO line analysis of associated large-scale structures (Yan et al. 2021). Since the uncertainty of S187's GAIA-based distance estimation is still not given we adopt the 1.4 ± 0.26 kpc distance. The H II region is surrounded by a molecular and atomic gas shell (Joncas et al. 1992; Arvidsson & Kerton 2011). A number of young stellar objects were detected towards the shell (Kang et al. 2017; Richards et al. 2012). Three sources with maser emission were also detected including two OH (Engels & Bunzel 2015) masers and an

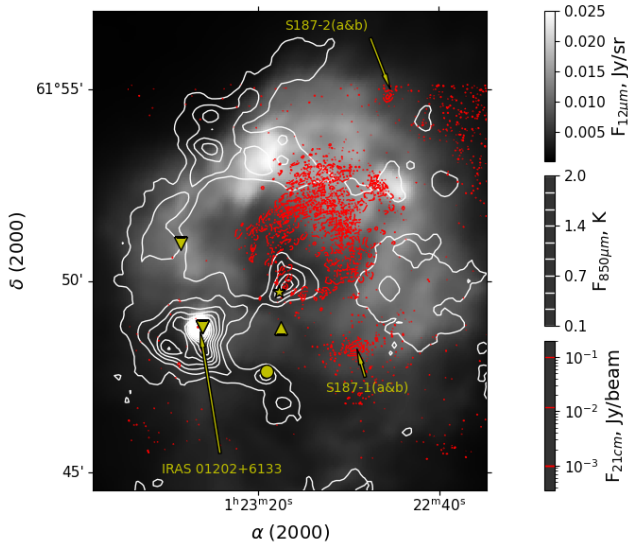


Figure 1. The structure of the S187 complex. The 1420 MHz GMRT continuum is in red contours, tracing the ionized gas. Bright red spots are related to radio galaxies (S187-1(a&b) and S187-2(a&b)). The red contours near S187-1(a&b) are caused by limited dynamical range. The noise on the top-right corner is caused by primary beam correction. The $12\mu\text{m}$ WSSA image is shown in grayscale tracing the dust in shocked gas. White contours represent SCUBA $850\mu\text{m}$ emission tracing cold dust in molecular material. The water maser (Sunada et al. 2007) is marked as a triangle and the OH masers from Engels & Bunzel (2015) are marked as reversed triangles. S187 NIRS 1 is shown as a circle and S187 H α as the star.

H₂O maser (Valdettaro et al. 2001) associated with a CH₃OH maser (Slysh et al. 1999), indicating ongoing star formation in the shell. Two compact radio sources were reported as known radio-galaxies (Snell & Bally 1986; Richards et al. 2012). They were misinterpreted as UC H II regions (Israel 1977) and have historical names S187-1(a&b) (NVSS 012258+614815, ABG85 94) and S187-2(a&b) (NVSS 012250+615451).

The formation of IRAS 01202+6133 ($M \sim 21 M_{\odot}$, $L \sim 5600 L_{\odot}$) is argued to have been triggered by the expansion of the S187 H II region (Kang & Kerton 2012). A pre-main-sequence object S187H α was discovered by Zavagno et al. (1994) with a mass of $25 \pm 12 M_{\odot}$ nearby to IRAS 01202+6133. A ^{12}CO outflow is associated with S187H α (Zavagno et al. 1994). A molecular hydrogen outflow driven by T Tauri star S187 NIRS 1 (S187:SCP 2) reported in Salas et al. (1998). The H₂O (Henkel et al. 1986; Han et al. 1995; Palagi et al. 1993; Valdettaro et al. 2001) and class II CH₃OH maser (Slysh et al. 1999) sources are located nearby. The existence of such objects is evidence of ongoing star formation in the shell. An OH maser (Engels & Bunzel 2015) was also detected to the north of IRAS 01202+6133, but we are not aware of any special study of the associated YSO. The dense molecular gas properties were discussed by Zinchenko et al. (2009); Kang & Kerton (2012) (see also references therein). The molecular part of the shell was observed in ^{12}CO , C¹⁸O and ^{13}CO (1–0) and discussed in Arvidsson & Kerton (2011), with the total mass estimate of about $7600 M_{\odot}$.

A multifrequency study of S187 and its environment was performed by Joncas et al. (1992), including H I data with $1'$ angular resolution and 1.32 km s^{-1} spectral resolution at 4.9 K sensitivity. According to Joncas et al. (1992), the H II region is interacting with the surrounding neutral gas. The ionised region is surrounded by the shell containing the H I counterpart. The atomic gas distribution

is inhomogeneous, has a systematic velocity gradient and the total mass is $70 M_{\odot}$. The associated YSO population is reported by Kang et al. (2017); Snell & Bally (1986). Two types of dust populations with grains larger than $0.004 \mu\text{m}$ were detected in infrared emission (Joncas et al. 1992). In summary, the S187 environment is a good target to study the interaction of the ionized, atomic and molecular gas and its impact on star formation.

In this study, we present new GMRT HI and continuum observational data of the S187 region including two molecular cores (S187 NE & S187 SE) in the shell around the H II region that illustrate different phases of the interaction between molecular, atomic, and ionized gases. Section 2 presents the observational data at 21 cm, radio continuum, molecular lines HCO⁺(1–0), CS(2–1), ^{12}CO (1–0), ^{13}CO (1–0), C¹⁸O(1–0), and infrared data from WISE. Section 3 describes the observational results derived from these datasets. More details and the analysis of the observations are presented in Section 4. Also, we discuss our results in Section 5, and at the end we give the conclusions.

2 OBSERVATIONS AND ARCHIVAL DATA

2.1 21 cm line and radio continuum

The 21-cm data were obtained using the Giant Metrewave Radio Telescope (GMRT, project 26_012) during 2014 September 4–5. The legacy GMRT backend was configured to the 8.138 kHz (1.72 km s^{-1}) resolution and the 4166.7 kHz bandwidth. 3C48, 0102+584, 0217+738, and 3C147 were observed as calibration sources. 3C48 was used as a bandpass and fluxscale calibrator, 3C48, 0102+584, and 0217+738 as phase calibrators. Absorption features were detected towards 3C147, 0217+738, 0102+584. The channels affected by absorption were excluded during the calibration. Around 30% of the data were manually flagged mostly due to radio frequency interference in some baselines. The calibration was performed in CASA (McMullin et al. 2007). A strong compact radio source NVSS 012258+614815 in the source field was used for phase self-calibration. The continuum image RMS noise was 0.1 mJy/beam at the field centre for Briggs-weighted image restoring (beam: 2.28×2.1 arcsec, PA -2°). A UV-tapered continuum image was also produced to achieve the spatial sensitivity with a beam of 8.3×7.0 arcsec, PA -10° and 0.7 K RMS.

Two spectral cubes were processed with different restoring beams. One with the Briggs weighted beam (2.7×2.2 arcsec, PA -13°) and the other with the uv-tapered naturally weighted (8.11×7.28 arcsec, PA 7.4°) beam to achieve sensitivity to the extended structures. We performed uv continuum subtraction for the uv-tapered data and combined it with the WSRT CGPS H I line survey (Taylor et al. 2003) using CASA SDINTIMAGING (Rau et al. 2019) to fill the flux loss. The standard CLEAN procedure was applied with cutoff limit of 10 mJy/beam. The tapered combined image has a per-channel RMS noise around 3 K, the Briggs weighted GMRT-only datacube has a sensitivity of 1 mJy/beam (80 K) RMS noise per channel.

2.2 Molecular lines

New HCO⁺(1–0) observations were carried out in 2021 April with the 20-m telescope of the Onsala Space Observatory (OSO) (project O2020b-02). The 3 mm dual-polarization receiver with a SIS mixer was used (Belitsky et al. 2015). A Fast Fourier Transform spectrum analyser with a 76 kHz frequency resolution was used. The spectrometer gives a velocity resolution of $\sim 0.26 \text{ km s}^{-1}$ at 89.2 GHz. To

obtain high-sensitivity data, the signals from two polarizations were co-added during the reduction process, which provided an increase of sensitivity by a factor of $\sqrt{2}$. The observations were performed in the frequency switching mode. The system noise temperature varied in the range of $\sim 170 - 290$ K depending on weather conditions. The main beam efficiency was ~ 0.44 for elevations of $\sim 30^\circ$ at which the source was observed. The full beam width at half maximum (FWHM) of the OSO-20m telescope at 86 GHz is 43 arcsec. Pointing and focus were checked regularly by observations of SiO masers. Mapping was done with a 20 arcsec grid spacing. The line data were processed using the CLASS program from the GILDAS package¹, the XS software², and our original routines.

The CS(2–1) line was observed by Joncas. It was obtained on 1987 November 30 using the 14 m telescope of the Five College Radio Astronomy Observatory (FCRAO) observatory. The data were not previously published. The telescope was equipped with a cooled 3 mm receiver connected to a digital spectrum expander as the back-end with resolution of 50 kHz and 256 channels. The weather was clear, and typical system temperature around 400 K. The individual scans were processed using the IRAF software (Tody 1986) and mapped using our scripts based on ASTROPY package (Astropy Collaboration et al. 2013). The spectral resolution is 0.25 km s^{-1} and the angular resolution is 45 arcsec. The beam efficiency was taken from FCRAO GRS as 0.48 (Jackson et al. 2006). We assume the same flux uncertainty of 15% as in this paper. This data has a larger coverage ($1^{\text{h}}23^{\text{m}}51^{\text{s}}.2 +61^\circ51'00''9$ centre, 10 arcmin square field) than the CS(2–1) observations reported in Zinchenko et al. (2009).

Observations of the ^{12}CO (1–0), ^{13}CO (1–0) and C^{18}O (1–0) lines were kindly provided by Kim Arvidsson and Cris Arvidsson and were done with the 14 m FCRAO telescope, processed by C. Brunt with the spectral resolution of 0.25 km s^{-1} and angular resolution of 46 arcsec (Arvidsson & Kerton 2011). We also used ^{12}CO (1–0) data from FCRAO CGPS to study the extended structures around the S187 region. The HCO^+ (1–0) data towards IRAS 01202+6133 are from Zinchenko et al. (2009). They were obtained at the Onsala observatory. The spectral resolution is 84 m s^{-1} with a 0.4 K RMS noise.

2.3 IR data

We used the WISE archive data images to study the dust emission in the region. The 2MASS (H and Ks) (Cutri et al. 2003) and WISE (i.e., W1, W2, and W3) photometric data we utilized to classify YSOs in the area and Spitzer IRSA, unWISE (Meisner et al. 2017) and WSSA (Meisner & Finkbeiner 2014) archive data for presentation purposes. We also used the SCUBA data archive for a $850 \mu\text{m}$ image that was previously described in Arvidsson & Kerton (2011).

3 OBSERVATIONAL RESULTS

We present the 1420 MHz continuum and the 21-cm line data in absorption and emission. We discuss the compact features first and then concentrate on the extended structures. We also present molecular gas emission morphology in addition to those published in Arvidsson & Kerton (2011).

3.1 Radio continuum

The structure of the 1420 MHz continuum emission is consistent with previous studies (Snell & Bally 1986; Arvidsson & Kerton 2011). Six compact sources are detected in the field, five of them are near the S187 H II region (Fig. 1), four of them are identified in the NVSS catalog. The fluxes are given in Table 1.

The parameters were estimated using CASA 2D Gaussian feature fit. The brightest one, NVSS 012258+614815 (S187-1) is located near the S187 H II region. It is known as a radio galaxy (Snell & Bally 1986; Arvidsson & Kerton 2011). We resolve it in two separate compact sources and an elongated extended weak structure. The compact sources are separated by 10 arcsec (Fig. 2), with brightness of $24000 \pm 120\text{K}$ (S187 1a) and $14300 \pm 120\text{K}$ (Fig. 3). NVSS 012250+61545 (S187 2) is also split into two compact features. A weak point source with a flux of $0.67 \pm 0.14 \text{ mJy}$ is detected towards IRAS 01202+6133. This source is associated with the Class I protostar reported in Kang & Kerton (2012). A water vapor maser is present near IRAS 01202+6133 as demonstrated by Zinchenko et al. (1998). This source is a region of high-mass star formation (Kang & Kerton 2012). To the best of our knowledge, no radio continuum emission was previously reported towards IRAS 01202+6133. Thus, there is no data to estimate the spectral index. The continuum point source can represent an UC H II region.

S187-1a&b are brighter than the extended H II region requesting high quality calibration. The UV-tapered continuum image IS shown in Fig. 1 in red. The emission associated with S187 is not homogeneous. The shape is close to a ball-like structure overlaid with a curved feature. This feature is bordered by $850 \mu\text{m}$ SCUBA emission associated with the parental cloud of IRAS 01202+6133, as seen in Fig. 1. There are two weak peaks in radio continuum emission, located near the SCUBA $850 \mu\text{m}$ and WISE $12 \mu\text{m}$ peaks (Fig. 1). We associate these features with PDRs and call them S187 PDR1 and S187 PDR2, (coord. in Table 2, see Fig. 4). The SCUBA $850 \mu\text{m}$ emission is detected near the IR peaks associated with PDR1 and PDR2. Weak continuum emission surrounds the S187 PDR2 from north and south (Fig. 1, Fig 4, center; , Fig 4, right). Such morphology is an argument for a small, density bounded zone bordered or surrounded by the leaking ionising emission and gas.

3.2 The H I data

Using the combined GMRT+CGPS data we are able to obtain full-scale high-resolution datacubes of the atomic hydrogen lines. From the GMRT data only we obtain high-contrast absorption profiles towards S187-1(a&b). The 21-cm emission and absorption line profiles are shown in Fig. 3. These profiles contain at least 8 spectral features. The emission features at $[-5; -20] \text{ km s}^{-1}$ are located near the S187 H II region, at the same velocities as molecular gas traced by ^{12}CO (discussed later). These velocities argue for an Orion arm membership (Joncas et al. 1992).

We resolved NVSS 012258+614815 as two compact sources giving the possibility for highly accurate estimation of the optical depth and column density of the absorbing gas (see next section). Other compact sources are too weak to detect absorption between continuum and hydrogen line brightness levels ($\sim 100 \text{ K}$) in our beam.

The 21-cm line emission from the combined CGPS+GMRT data are shown as channel maps in Appendix B (Fig. B1). The maps are overlotted with black contours which show the ^{12}CO (1-0) emission from Arvidsson & Kerton (2011). The observed structures are in good consistency with those discussed by Joncas et al. (1992) despite an order of magnitude improvement in resolution (from 60

¹ <http://www.iram.fr/IRAMFR/GILDAS>

² <https://www.chalmers.se/en/researchinfrastructure/oso/radio-astronomy/Pages/software.aspx>

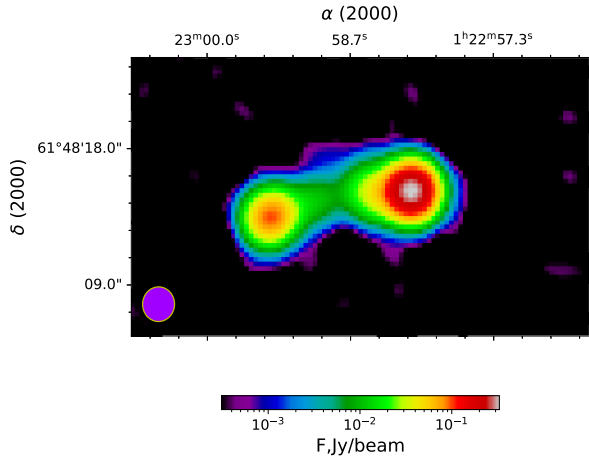


Figure 2. Closeup view of NVSS 012258+614815 (S187-1 a&b) in the GMRT 1420 MHz continuum. The beam is shown in the lower left corner. Fluxes are in logarithmic scale.

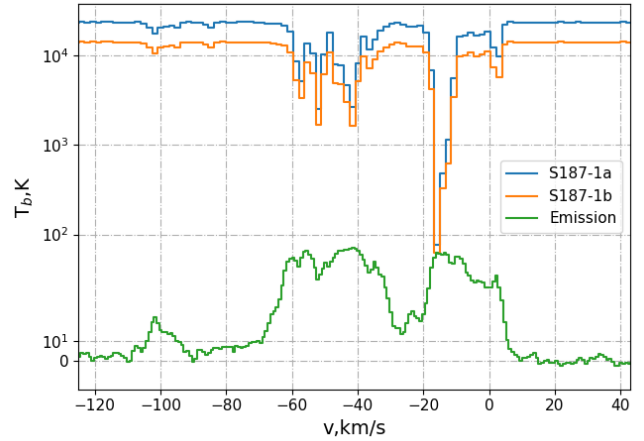


Figure 3. The H I spectra towards NVSS 012258+614815 (a and b). Emission spectra are extracted from the CGPS survey inside the 1' circle around the galaxy position. The absorption profiles are obtained from the GMRT data. The brightness values below 50 K are shown using a linear scale those above 50K with a logarithmic scale.

Table 1. Continuum sources properties and parameters estimated using the CASA 2D Gaussian feature fit.

Source	Coordinates, J2000	Flux at 1420 MHz, mJy	Size, deconvolved: major,minor,p.a., arcsec
S187-1a	01 ^h 22 ^m 58 ^s .11304(.0006)+061°48'15".188(.0037)	386.4(2.5)	1.27(0.02)x0.38(0.063)x91(2.5)
S187-1b	01 ^h 22 ^m 59 ^s .39627(.002)+061°48'13".52(.013)	116.7(0.8)	1.4(0.08)x0.35(0.2)x112(4.9)
S187-2a	01 ^h 22 ^m 51 ^s .346(.0017)+061°54'48".22(.015)	13.7(0.3)	1.3(0.1)x0.58(0.16)x144(7.4)
S187-2b	01 ^h 22 ^m 50 ^s .91(.02)+061°54'51".93(.14)	7.9(0.7)	4.42(0.4)x3.4(0.4)x131(22)
IRAS 01202+6133	01 ^h 23 ^m 33 ^s .36(.012)+061°48'48".09(.15)	0.67(0.14)	point
NVSS 012355+614404	01 ^h 23 ^m 54 ^s .1(.012)+061°43'57".73(.08)	1.8(0.24)	point
S187	01 ^h 23 ^m 04 ^s .8(.1)+061°51'41".2(.4)	1200(20)	175.62(3.6)x141.3(3)x162(4)

Table 2. Molecular and infrared sources sizes estimated using the CASA 2D Gaussian feature fit. The integrated C¹⁸O intensity image is marked as \int C¹⁸O.

Source	Coordinates, J2000	Size: maj,min,bpa, arcmin	source
S187-NE	01 ^h 23 ^m 29 ^s .9(1.37)+061°54'28".8(8.9)	4.1(0.4)x3.65(0.2)x129(7.5)	\int C ¹⁸ O
S187-SW	01 ^h 23 ^m 30 ^s .5(1.2)+061°48'49".7(7.0)	4.2(0.4)x3.4(0.3)x93(17)	\int C ¹⁸ O
S187-PDR1	01 ^h 23 ^m 17 ^s .93(.03)+061°53'10".34(.2)	3.12(0.1)x2.00(.006)x128(0.29)	12 μ m WISE
S187-PDR2	01 ^h 22 ^m 50 ^s .2(.02)+061°52'28".8(.1)	2.04(.008)x1.27(.005)x69.4(.3)	12 μ m WISE
HI subbubble	01 ^h 23 ^m 39 ^s .8(.1)+061°51'37"(1.5)	3.9(.1)x4.1(.1)x90	12 μ m WISE

arcsec to 8 arcsec) and a factor of 3 improvement in sensitivity (from 0.7 to 0.3 mJy/beam) in restored beam. The H I emission towards S187 is not homogeneous, the channel maps reveal spatially and kinematically connected structures up to scales of ~ 0.6 pc. The features that are spatially related to the H II region are detected from -20.7 to -3.5 km s⁻¹. At the edges of the velocity range, the emission is located towards the centre of the H II region tracing the parts of the shell walls oriented with the motion parallel to the line of sight. As shown in Fig. 4, the integrated H I line emission correlates well with the 5.8 μ m Spitzer emission. The local peaks of the H I line are slightly shifted from the infrared data peaks outwards of centre of the H II region. The emission region has a shape close to a circle with inhomogeneous borders except for the north-east direction, where the border is curved inside.

3.3 Molecular lines

The shell around S187 has a molecular counterpart (Joncas et al. 1992; Zinchenko et al. 2009; Arvidsson & Kerton 2011). It consists of dense regions with molecular cores and more diffuse, surrounding gas generally related to the ionized region envelope. We used the CS(2–1) and HCO⁺(1–0) observations as tracers of the dense regions. The molecular gas emission in the CO isotopologue lines are presented AS channel maps (Figures in appendix B, B2, B1, B3). The ¹²CO emission lines are detected all over the field. The ¹³CO emission region is more extended than the H I associated with S187. The C¹⁸O emission is usually optically thin, tracing the column density of the molecular gas. We associate it with the dense cores in the molecular shell at different stages of evolution (discussed below). There are two peaks detected at different velocities, hereafter called S187 SE, the parental cloud associated with IRAS 01202+6133 and

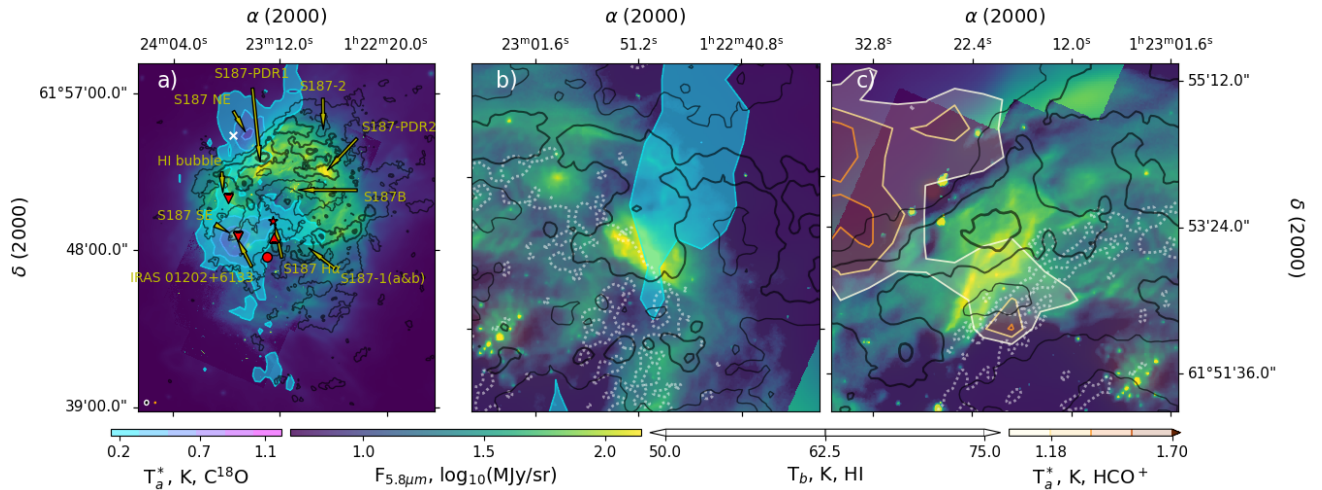


Figure 4. *a)* The observed features in the S187 complex. Background image is the Spitzer $5.8\mu\text{m}$ image overlaying the WISE WSSA $12\mu\text{m}$ image (in green and yellow shades). The C^{18}O average intensity in the $[-17.5, -12]$ km/s range is shown in blue filled contours while black contours represent the 21-cm line emission in the same velocity range. The contour width is increasing towards the brighter emission. The beams (46 arcsec, 8 arcsec, and 8 arcsec for the C^{18}O , H I and 1420 MHz continuum, respectively) are shown in the lower left corner of the image. the position of S187 H α is marked as a red star. A white cross marks the HCO^+ line intensity peak position. The other marks are the same as in Fig. 1. *b)* Close-up picture of S187 PDR2. The image scheme is the same as for *a)*, except the velocity range is $[-13, -10]$ km/s. Light gray dotted contours represent 1420 MHz continuum emission at a 7K intensity level. Declination tick marks are placed at $+061^\circ 51' 24''$ and $+061^\circ 51' 36''$. *c)* Close-up picture of S187 PDR1. The image scheme is the same as for *b)*, except the line which is HCO^+ the velocity range is $[-17, -13]$ km/s since the S187 PDR1 central velocity is different.

S187 NE. S187 NE spatially and kinematically correlates with the ^{12}CO peak while S187 SE does not. At the velocity of S187 SE ($\sim -15 \text{ km s}^{-1}$) the ^{12}CO line is mostly homogeneous (Fig. B1). The bright peaks of the C^{18}O emission strongly anti-correlate with the H I data, most strongly towards S187 SE. The molecular emission elongates towards the S187 exciting star cluster, a small peak of the H I emission is detected towards the centre of the H II region. No $12\mu\text{m}$ WISE feature is detected towards or near S187 SE. This absence can be a projection effect on the line of sight meaning that the molecular gas is not related to the S187 shell, but the anti-correlation between H I and C^{18}O suggests that the molecular gas of S187 SE is embedded into the atomic medium. No H I emission is detected at the position and velocity of S187 SE C^{18}O and HCO^+ peaks. No cometary ^{12}CO molecular emission is detected around the C^{18}O peak. The peak of H I gas, at the -11 km s^{-1} is located towards the molecular emission peak near the S187-H α object.

The CS line properties (Fig. 5) are consistent with those in Zinchenko et al. (2009). In addition we detect an extended feature with a line brightness of $\sim 0.6 \pm 0.2 \text{ K}$ and central velocity of -15 km s^{-1} . The feature extends to the north of IRAS 01202+61133. The CS and HCO^+ peaks are shifted from the C^{18}O peak outwards of S187B. The HCO^+ observations towards S187 NE have similar properties. Two features also exist. The line peak is centred at $1^{\text{h}}23^{\text{m}}34^{\text{s}}.7 + 61^\circ 54' 38''.8$ with maximum intensity of $2.8 \pm 0.2 \text{ K}$ and velocity of $-16 \pm 0.3 \text{ km s}^{-1}$ and a $\sim 2 \text{ km s}^{-1}$ line FWHM. (Fig. 4, a) The extended feature has a $\sim 3 \text{ km s}^{-1}$ FWHM centered at $-15 \pm 0.3 \text{ km s}^{-1}$ and peak intensity of $1.7 \pm 0.25 \text{ K}$. The extended feature is located towards the S187 PDR1. The profile has non-gaussian features. The line profiles are shown in Fig. 5.

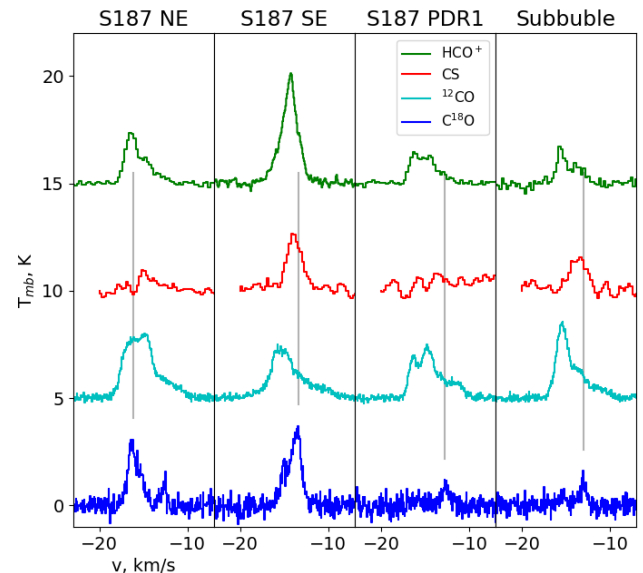


Figure 5. The $\text{C}^{18}\text{O}(1-0)$, $^{12}\text{CO}(1-0)$, CS(2-1) and $\text{HCO}^+(1-0)$ spectra towards some positions of the S187 shell. The $^{12}\text{CO}(1-0)$ intensity is divided by a factor of 7. Vertical lines mark the C^{18}O peak intensity.

4 PHYSICAL PROPERTIES ESTIMATION

4.1 The properties of the H I gas

The presence of two closely-located strong background sources (S187-1a&b) gives the possibility for accurate measurement of the absorption profile of the cold neutral hydrogen gas. We used GMRT-only data (beam: 2.7×2.2 arcsec, PA -13°) for optical depth profile extraction. Using the emission line from the CGPS survey we are able to estimate the spin temperature of the neutral hydrogen. We assume

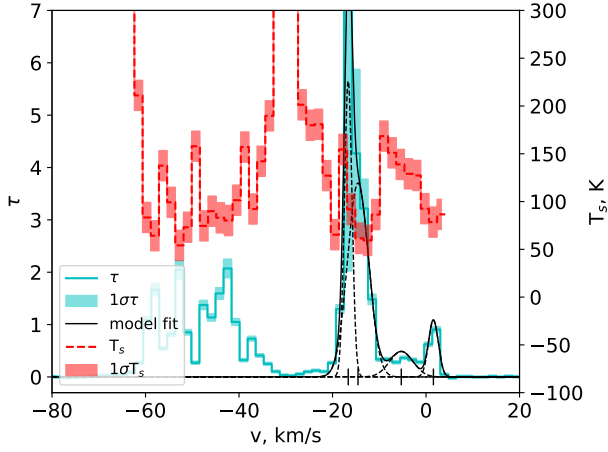


Figure 6. Optical depth and spin temperature profiles towards S187-1(a&b). The flat-layer model fit is shown as a black solid line and the individual layers emission profiles are shown as dashed lines. The velocity of each layer is shown by a vertical mark.

that the properties of the background galactic atomic gas does not vary significantly across the GMRT field.

We estimate the optical depth towards S187-1(a&b) from the two H I absorption spectra:

$$\tau(v) = -\ln \left[\frac{T_{br}^a(v) - T_{br}^b(v)}{T_c^a - T_c^b} \right], \quad (1)$$

where $T_{br}^a(v)$ and $T_{br}^b(v)$ are the observed line temperatures towards the S187-1 components *a* and *b* shown in Fig. 3. T_c^a and T_c^b are the continuum brightness temperatures of the components derived from the same spectra. We suppose the same filling factor for both components separated by 9.5 arcsec (0.05 pc) and the same optical depth for the absorbing gas towards both sources. The components *a* and *b* have nearly the same size (Table. 1). The sizes estimated as $1 \times 3''$ and $1 \times 2''$ (5 & 15 GHz) for *a* and *b*, respectively (Snell & Bally 1986). With this estimation we also exclude calibration errors between different instruments and missing flux related to the absorption-emission optical depth estimation (Nguyen et al. 2019), where absorption spectra are acquired by an interferometer and emission spectra by single dish. The spin temperature is calculated using emission spectra averaged near S187-1(a&b) from the CGPS survey observations over a $1'$ region excluding the S187-1 area:

$$T_s = T_{em} / (1 - e^{-\tau(v)}),$$

where T_{em} is the line temperature from the CGPS survey (see Fig. 3) and τ is taken from Eq. 1. The resulting profiles are shown in Fig. 6. The high uncertainty of the optical depth estimation at -17.5 km s^{-1} may be caused by two factors. First, the presence of extended emission at that channel increases the RMS and thus the uncertainty of the estimation. Second, S187-1 a and S187-1 b have similar intensities due to the high optical depth which leads to a smaller value of the numerator in the expression 1 and thus higher uncertainties. It is worth noting that T_s and τ estimations are the line of sight ensemble-averaged values. We do not take into account a possible beam dilution that may increase the spin temperature value.

To estimate the properties of the atomic hydrogen layer in the entire S187 shell we fit a flat-layers model to the emission spectra from the combined data. The brightness temperature T_b emitted by

layer *i* is

$$T_b^i(v) = T_s^i(1 - e^{-\tau_i(v)}) + T_b^{i-1}(v)e^{-\tau_i(v)}, \quad (2)$$

where

$$\tau_i(v) = \tau_i \times \exp(-(v - \Delta v_i)^2 / (2\sigma_i^2)), \quad (3)$$

is the optical depth profile of layer *i*, τ_i is the peak optical depth of layer *i*, Δv_i is the Doppler velocity and σ_i is the Doppler width of the optical depth profile of the same layer. The total number of layers is defined by the number of components in the Gaussian decomposition of the optical depth profile derived from the absorption spectra and was equal to 4. The velocity of the layer decreases with *i*. We assume that the outer layers represent outer parts of the Galaxy.

We analysed the combined CGPS+GMRT data using the algorithm described in Appendix A which combines iterative least squares fitting whose initial conditions are estimated by k-Nearest Neighbors (kNN). Based on the analysis of the spectral profiles in different positions of the map we constrained some parameters of the different layers. The component at the velocity of $\sim 3 \text{ km s}^{-1}$ does not vary significantly and their parameters are fixed. We also fixed the velocity, the Doppler width and the spin temperature of the component at $\sim -5 \text{ km s}^{-1}$. These components are probably related to other galactic structures. Summarizing, nine parameters are varied, ($T_s^i, \tau_i, \Delta v_i, \sigma_i$) for each component and τ_i for one component.

Using the constraints described above we fitted the model to the different positions. The results converged in three passes. The optimal number of the nearest neighbors is estimated as 5.

As described in the next section, the H I gas has the internal kinematics of an expanding bubble, so the assumption of a Gaussian line width in this object is far from ideal. We estimate the column density of the atomic layer from the following equation using the fit results and the kNN regression:

$$N_{HI} = 1.823 \times 10^{18} \text{ cm}^{-2} \int \frac{\tau T_b(v)}{[1 - \exp(-\tau(v))]} dv, \quad (4)$$

from Saha et al. (2018). Here T_b is the brightness temperature of the model component and τ is from Eq. (3). The column density map of the atomic gas related to S187 is shown in Fig. 7. The atomic gas associated with S187 is surrounded by ambient gas. We subtract the mean column density of the ambient gas and calculate the mass of the H I gas related to S187 as $260 \pm 56 M_\odot$. The ambient gas column density is estimated by using the flat-layer model fit in the outer regions where no ^{13}CO and $12 \mu\text{m}$ WISE emission was detected. Using the model fit and assuming the temperature broadening we estimated the upper limit of the kinetic temperature of the atomic gas $T_{kin} < 1000 \text{ K}$. In the case of thermalization, the H I kinetic temperature should be equal to the spin temperature. The median temperature over the S187 shell temperature is 50 K. The peak of the spin temperature is located towards S187 PDR1 with a value of 110 K. The FWHM of the PV diagram size is ~ 10 arcmin which we adopt as the H I shell size.

The HI column density is well-correlated with the bright $12 \mu\text{m}$ WISE emission, which is tracing hot dust and polycyclic aromatic hydrocarbons (PAH) in PDRs, but with significant deviation from a linear regression. Negative correlation with the $12 \mu\text{m}$ WISE emission is present in the $[0, \sim 0.0015] \text{ Jy/sr}$ WISE flux range. The related points are located at the periphery and probably caused by a fraction of the atomic gas not being related to S187. The determination coefficient $R^2=0.26$ is relatively low and caused by non-systematic deviation from the linear regression. This deviation exceeds the estimated uncertainties and may trace the different excitation and PAH

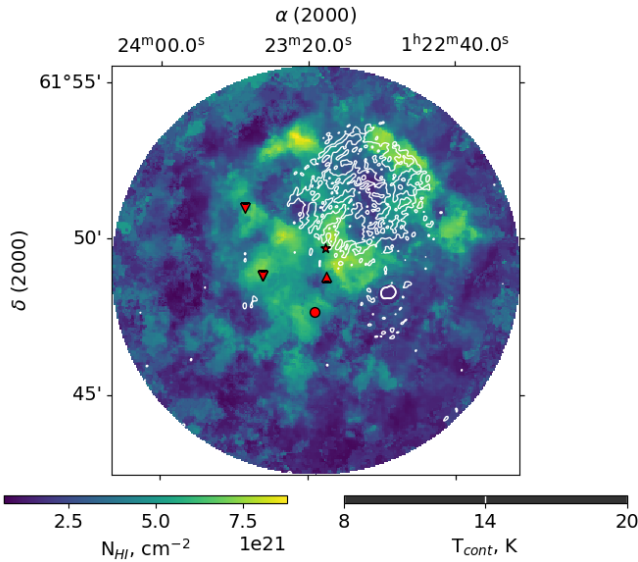


Figure 7. The atomic gas column density map towards S187. The white contours represent continuum 1420 MHz emission. The marks are the same as in Fig 4.

generation conditions. It is possible that not all atomic gas is produced by photo-dissociation of the S187 molecular shell.

4.1.1 Atomic gas clumps properties

We analysed the H I datacube using the FELLWALKER algorithm (Berry 2015). The cutoff limit was set to 7 times the RMS and the $[-19, -5]$ km s⁻¹ range is used. The results are shown in Fig. 8 and in Fig B1. We detect ~ 100 artefacts associated with the S187 atomic shell. We assume that the detected artefacts are the inhomogeneities of the atomic layer or fragments. Most of the fragments are concentrated at the shell periphery and correlate well with the 4.6 and 12 μ m WISE emission. Groups of small ones are located near the S187 PDR1, S187 PDR2 and S187 SE borders. 5% of the fragments are smaller than the double beam size, most of the fragments are resolved.

We estimate masses from the column density ($N_{HI} = 1.823 \times 10^{18} \text{ cm}^{-2} \int T_b dV$) and the geometric sizes of the fragments under the assumption of low optical depth (Wilson et al. 2012). The fraction of the optical depth concentrated in the fragments compared to into the interfragment medium is unknown so we consider it as the lower limit mass estimation. The fragment size along the line of sight is unknown and is assumed to be the mean value of sizes in the plane of sky. The results are shown in Fig. 9. The mean mass of the fragment is $1.14 M_\odot$. The total mass of the fragments estimated as $\sim 114 M_\odot$. Alternatively, the upper limit of fragment masses can be estimated under the assumption of the same optical depth as for the flat-layer model. This assumption gives nearly the same total mass of the fragments as for the entire shell ($\sim 240 M_\odot$). The actual fragment masses should lay between these values. Typical volume density is around $\sim 5.4 \times 10^4 \text{ cm}^{-3}$ for optically thin limit. Detected fragment sizes vary from 0.03 pc to 0.23 pc. The size is estimated as standard deviation of individual pixels calculated at 1.4 kpc distance, weighted by intensity. Our data indicate a tight ($R^2=0.94$) power-law correlation between mass estimation and fragment size (Fig. 10). The power-law index for the mass-size relation is $k = 2.39 \pm 0.06$.

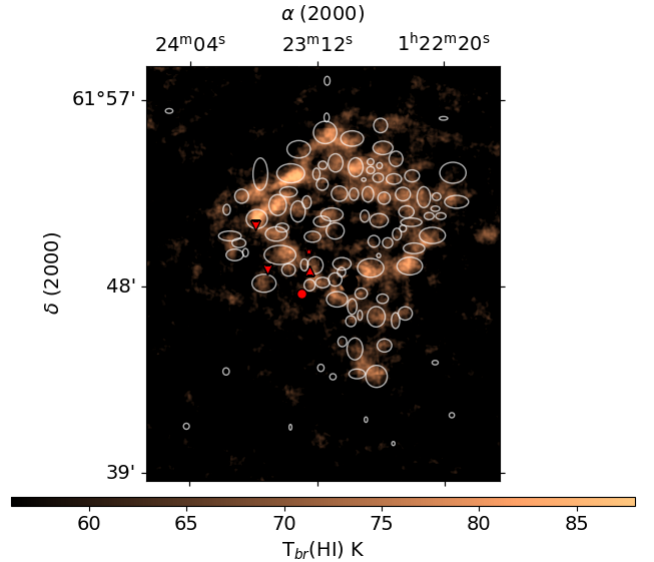


Figure 8. Spatial distribution of the H I fragments identified by the CUPID Fellwalker algorithm. The ellipses represent clump sizes (standard deviation around centroid). The H I peak intensity is plotted in the background. The marks are the same as in Fig 4.

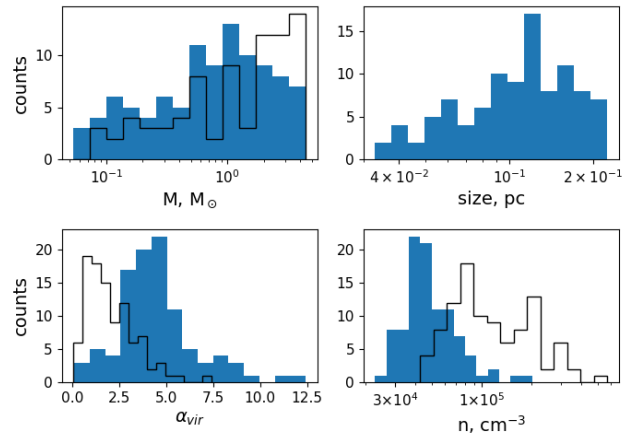


Figure 9. The properties of the fragments. *Upper left:* Individual fragment atomic gas mass histogram. *Upper right:* The fragment linear sizes histogram. *Lower left:* Virial parameters of the fragments. *Lower right:* the individual fragment volume density histogram. The filled bins correspond to the optically thin conditions and the unfilled ones are based on the flat-layer model. The bin step has a logarithmic base except for the lower left plot.

4.2 The molecular gas properties

We analysed the ¹³CO and C¹⁸O data from Arvidsson & Kerton (2011). The data has the same spatial and velocity coverage as H I combined data.

The CO isotopologues column density (N_{CO}) is estimated using Eq. 90 from Mangum & Shirley (2015). We assumed the same excitation temperature for the ¹²CO, ¹³CO and C¹⁸O lines and estimated it from ¹²CO data using Eq. (15.30) from Wilson et al. (2012). No ¹²CO emission associated with S187 SE is detected. For the S187 SE core, the excitation temperature is assumed as 9.5 K using the kinetic temperature estimation from Kang & Kerton (2012). The ¹³CO/¹²CO=0.0145 abundance ratio is calculated for the S187

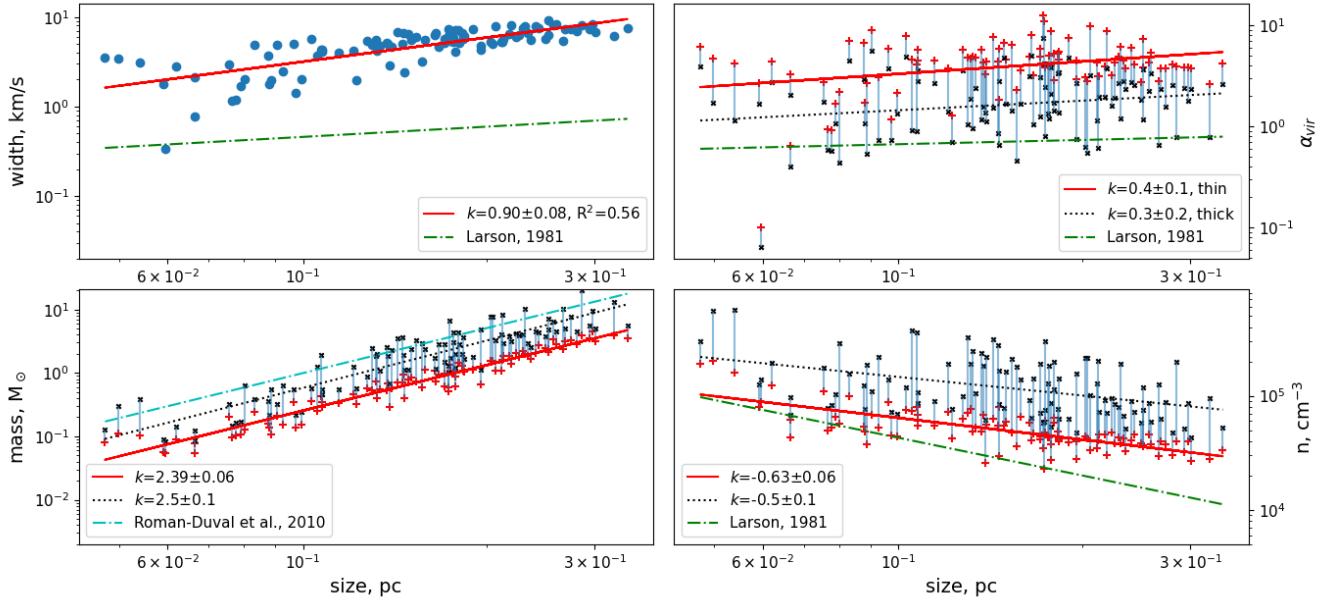


Figure 10. The correlations between fragment parameters. *Top left:* Linear size versus line width. *Top right:* Virial parameters versus linear size scatter. *Lower left:* Mass versus linear size. *Lower right:* Volume density versus linear size. The red pluses represent the values estimated in the optically thin limit and the black crosses represent the values estimated by using optical depth values from the flat-layer model fit results. The best fits are shown as red lines (thin) and dotted black line (τ from FLM). The same dependencies from Roman-Duval et al. (2010); Larson (1981) are shown by dash-dotted lines.

galactocentric distance of 9.27 kpc taking into account the galactic gradient of this ratio (Pineda et al. 2013). The CO to H₂ abundance ratio (7.7×10^{-5} for S187) is calculated using the galactocentric distance (Fontani et al. 2012). We estimated the shell mass using the ¹³CO data as 6400 M_⊙. Such estimate is close to the value from Arvidsson & Kerton (2011) derived from the same data.

We estimated virial parameters for the S187 SE and S187 NE cores using $\alpha_{vir} = 1.2\sigma^2 \sqrt{S_{eff}} / (10^{-3}M)$, where M is the core mass in M_⊙, σ in km s⁻¹ is calculated using the second moment of the ¹³CO line, $S_{eff} = \int T_b ds / T_b$ is the core area in pc² calculated from the ¹³CO T_b image, ds is the elementary area at a distance of 1.4 kpc (Kauffmann et al. 2013). The σ is ~ 1.4 and ~ 0.9 km s⁻¹, the mass is ~ 1200 and ~ 900 M_⊙ for S187 SE and S187 NE, respectively. The α_{vir} is estimated as 2.75 and 1.4 for S187 SE and S187 NE, respectively. The core masses are close to each other, the difference between virial parameters is caused by different line widths, that is probably caused by non-thermal motions in the cores.

4.3 Dust properties from the Akari-FIS & WISE data

We used data from the WISE and AKARI telescopes. The analysis is based on the 3.36, 4.6, 12.08, and 22.19 μ m images from the WISE survey (Wright et al. 2010) and on 65, 90, 140, and 160 μ m from the AKARI survey (Yamamura et al. 2010). Our aim was to identify different dust fractions with molecular and atomic spatial-kinematic features in the shell using the colours at different IR wavelengths. Spitzer data are also available towards S187, but it has poor coverage and quality. There is no Herschel observations for S187. For the analysis the WISE and AKARI-FIS data are used instead.

Prior to the analysis of the IR images of S187 and the calculation of the flux ratios, we cleaned the archival IR maps of point sources. They were removed from the images using an automatic cleaning procedure. The search and removal of point sources were carried out

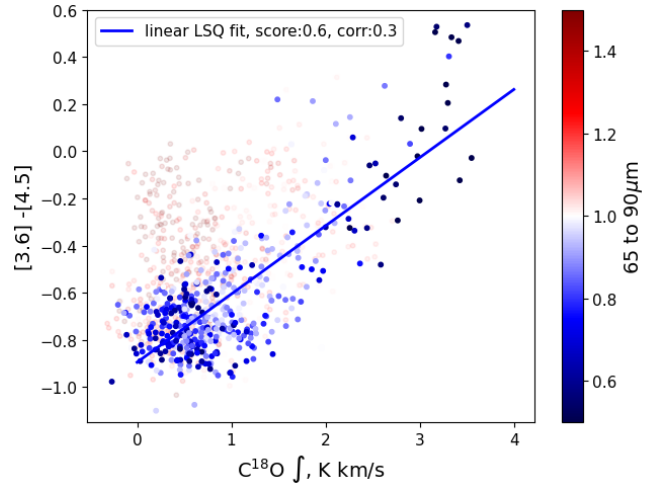


Figure 11. Scatter plot of the [3.4] – [4.6] WISE colour vs the C¹⁸O zero moment. Linear regression is estimated by Huber regression from Pedregosa et al. (2011). Dot colour indicates the 65 μ m to 90 μ m flux ratio value. Dots outside of the colorbar range and the C¹⁸O sensitivity limit are plotted as semi-transparent and are excluded from fitting.

in three subsequent stages depending on the brightness of the stars. More information can be found in Topchieva et al. (2017). The data were then convolved with a kernel as in Aniano et al. (2011) and reduced to the same pixel sizes and flux units.

The maps (Fig. 12) are plotted for different ratios of infrared wavelengths. At shorter wavelengths, the emission presumably comes from small grains, while emission in the 70 and 160 μ m bands comes from relatively large grains (Draine & Li 2007). The emission at 12.08 and 22.19 μ m may come from both stochastically heated small and hot large dust grains and PAH (Pavlyuchenkov et al. 2012)

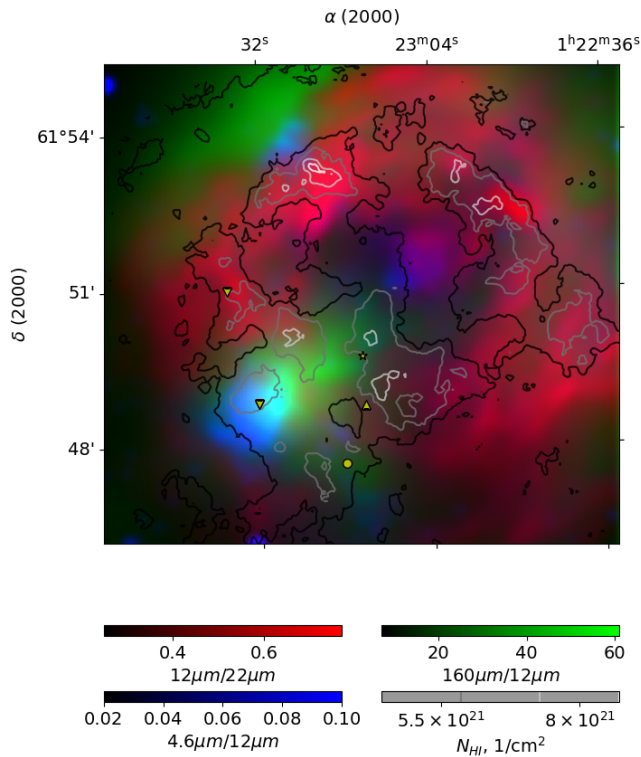


Figure 12. The S187 shell in the IR continuum. The WISE WSSA 12 μm image is in red. The H I column density is shown in contours. The marks are the same as in Fig 4.

PAH in 12 μm usually prevails (Reach et al. 2017). The 65 to 90 μm ratio is used as a large-grain temperature tracer (Draine & Li 2007).

Unlike Reach & Heiles (2021), we found that the the 12 μm to 22 μm ratio varies from point to point from 0.2 to 0.74 (See Fig. 12). The ratio correlates with the H I column density. The ratio variation can be associated with PAH/grains differentiation and processing (Reach & Heiles 2021). The ratio peaks are slightly shifted from H I column density peaks implying that PAH and H I are effectively generated on slightly different conditions.

We also analysed the [3.4]-[4.6] WISE colour and found that it is associated to the C¹⁸O integrated intensity. The colour is plotted in Fig. 11. We also plot the 65 μm to 90 μm ratio from AKARI data in colour. The colour correlate the C¹⁸O intensity under the linear regression. The determination coefficient $R^2=0.7$ for the regression line. The 90 μm flux dominating region is closer to the regression line than the 65 μm dominated region. The 90 μm emission is usually related to large dust grains (Draine & Li 2007) protected by dense gas represented by C¹⁸O emission.

4.4 Young stellar population

In order to identify infrared-excess sources or young stellar objects (YSOs) in our selected target area, we used the 2MASS (H and Ks) and the WISE (i.e., W1, W2, and W3) photometric data. Koenig & Leisawitz (2014) presented several schemes to identify YSOs, and two such schemes are utilized in this paper. We used one scheme based on the H–K_s and W1–W2 colour conditions, and the second one using the W1–W2 and W2–W3 colours. The results are shown in Fig. 13.

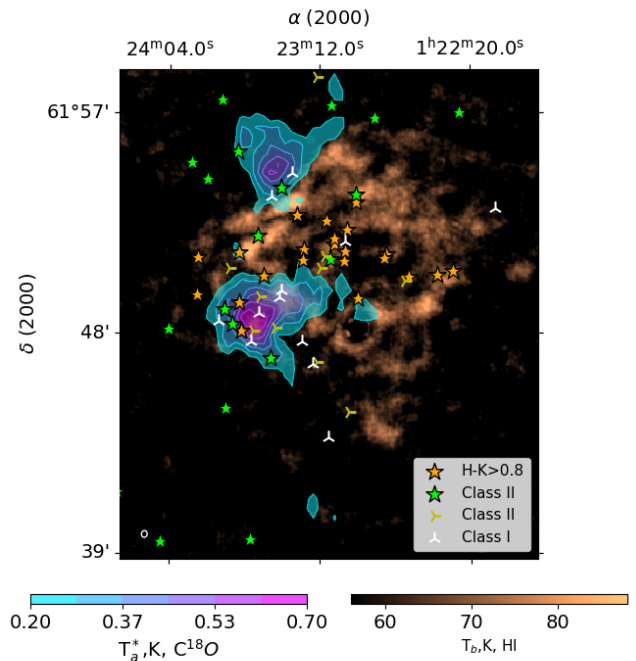


Figure 13. The distribution of the YSOs near S187. The background image represents the H I averaged emission in the $[-17.5, -12]$ km s^{-1} range. The blue contours represent the C¹⁸O emission averaged for the same velocity range.

5 DISCUSSION

Our data trace almost all aspects of the high mass star formation: the H II region with the ionizing cluster, the PDR regions with the photodissociated H I layer, the population of young stellar objects, and at least two molecular cores that could be at different stages of evolution. In Section 5.1 we discussed large-scale features that may be related to the origin of the S187 complex. In Section 5.2 we discussed the general distribution of the gas and YSOs around and in the H II region. In Section 5.3 we discussed the inner spatial-kinematic structure of the shell.

5.1 Large-scale features

One of the interesting feature that is probably not related to S187 is the existence of narrow absorption and emission HI features at $\sim 5 \text{ km s}^{-1}$ (Fig. 3 and 6). They are in principle "forbidden" in this quadrant by the rotation curve of the Galaxy (Joncas et al. 1992). The existence of this feature is interesting but its detailed analysis lies beyond the scope of this paper. Such features are usually explained by local streaming motions near the Sun caused by the Galactic density wave (Burton 1971). Another possible explanation can be large-scale kinematics caused by the expansion of a supernova remnant (Cichowolski et al. 2014). The picture of the surrounding medium is shown in Fig. 14 and is taken from the CGPS H I and ¹²CO (1–0) surveys (Taylor et al. 2003). A position-velocity diagram IS shown in Fig. 15. Two nearly circular structures traced in H I and ¹²CO are detected. Such PV features can be formed by the expansion of energetic bubbles. The feature at $\sim 5 \text{ km s}^{-1}$ is probably part of such a bubble. The "unusual" velocity can be explained by the "snow-plow" effect often accompanying such energetic phenomena.

We propose that these bubbles are related to supernova events. The northern one is probably caused by SNR G127.1+0.5 (Leahy &

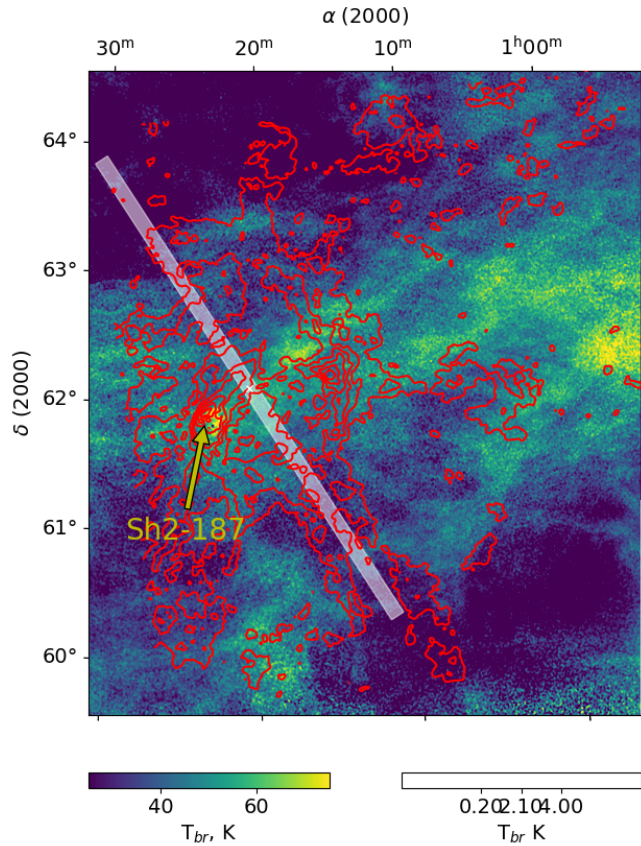


Figure 14. Map of the S187 surroundings. The averaged CGPS H I emission ($[-14$ to -17 km s^{-1}] range) is shown in the background. It is overlaid with the ^{12}CO emission averaged in the -5 to -17 km s^{-1} interval. The rectangle indicates the location of the PV diagram shown in Fig. 15. The crosses correspond to 0 and 2.2 degrees position offsets.

Tian 2006), and the southern one is probably related to the pulsar B0105+65 and the G126.1-0.8 shell (Cichowolski et al. 2014). We estimate the dynamical age from $t_{dyn} = \alpha R/V_{exp}$. $\alpha = 0.25$ for a radiative-driven expansion and $\alpha = 0.6$ for a shell created by the action of stellar winds. The inner radius of the atomic part of the shell is R and V_{exp} is the expansion velocity (Cichowolski et al. 2014). The northern bubble age is $t \sim 3.6 \times 10^5$ yr (radiatively driven) or $t \sim 8.8 \times 10^5$ yr (wind driven expansion) (Cichowolski et al. 2014). The southern bubble age is $t \sim 3.0 \times 10^5$ yr or $t = 7.15 \times 10^5$ yr for a radiative or wind driven expansion respectively, which gives relatively the same age for both SNR.

By this view S187 region is located at the intersection of the bubbles. the molecular gas appears only at ~ -12.5 km s^{-1} , on one side of the bubbles.

5.2 The shell

Using the data discussed in Sect. 3 we traced different parts of the expanding gas and dust surrounding the H II region. The overall picture is shown in Fig. 4. The channel maps of the H I emission compared with the CO isotopologue lines are shown in Figs. B1, B2, B3. Our observations indicate an expansion of the atomic gas related to the shell. The expanding part has an almost circular shape. It is centered on the H II region. The position-velocity diagram is shown in Fig. 16. The emission peaks can be associated with the shell walls,

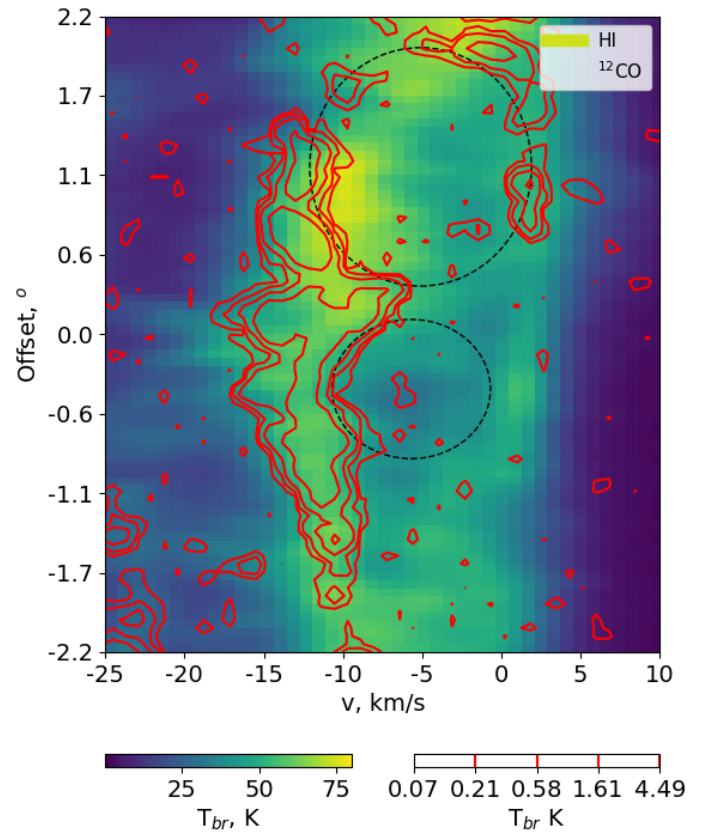


Figure 15. The position-velocity diagram of the atomic and molecular gas near the S187 region. The PV slice is shown on Fig. 14. Black ellipses indicate the probable SNR locations.

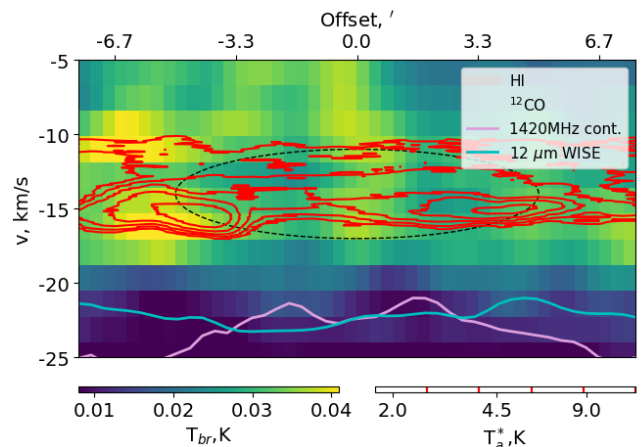


Figure 16. The position-velocity diagram of the atomic and molecular gas. Normalized IR and radio continuum profiles are plotted at the bottom. The ellipse represents inner border of the radially expanding shell. The PV slice is shown in Fig. 20 as the red box.

which are brighter near molecular emission peaks. The velocity of the H109 α line related to the H II region is -14.6 km s^{-1} (Joncas et al. 1992). It is close to the expanding layer centre velocity. The H I emission related to S187 is detected in the -21.5 to -8.5 km s^{-1} range

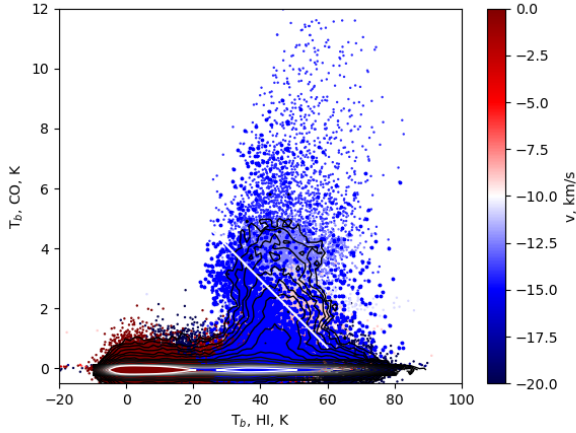


Figure 17. Scatter plot of the H I vs the ^{12}CO emission. The red-blue colour indicates the channel velocity. The scatter plot is overlaid with a 2D histogram shown by black contours. The possible correlation within the $[-15.1, -16.9]$ km s^{-1} range is shown as a white line.

(Fig. 16). The PDR atomic layer at the centre should expand directly towards and outwards with respect to the observer. As a result, no H I emission should be observed at ~ -14.6 km s^{-1} and towards the H II region. However, the H I emission is observed towards the zero offset in the PV diagram (see Fig. 16). This emission cannot be explained as line broadening of the Doppler-shifted wall. The source of the emission can be the atomic gas inside or outside of the sphere. The first possibility implies that neutral gas fragments remain within the H II region, that are not involved in a systematic expansion. The other possibility implies the presence of neutral atomic gas dissociated by leaking radiation from the H II region that is not involved in systematic motions either.

The channel-by-channel scatter plots of the ^{12}CO and H I data does not show linear correlation (see Fig. 17), except for the $[-17, -15]$ km s^{-1} range. In this range a sign of negative correlation is observed and shown as a white line. It may trace the molecular gas dissociation processes. In the remaining velocities, no sign of linear correlation is observed, probably resulting from the limited resolution of the molecular data. The shell's atomic mass estimate ($260 \pm 56 M_{\odot}$) is much higher than estimated in Joncas et al. (1992) ($70 M_{\odot}$, under the assumption of low optical depth from the absorption profile). Also, the absorption profiles (Fig. 3) indicate deeper absorption than reported in Joncas et al. (1992). Such difference arises due to the significant optical depth correction in our work. Without it both consistent. In addition, our approach is based on the observations of very compact sources. The atomic gas is highly fragmented, so the absorbing properties may vary on small scales. To our luck, the detected fragments have the sizes much larger (Fig. 9) than the S187-1(a&b) sizes and their separation. The estimate of the shell's atomic mass is small compared to the molecular gas mass in the shell ($6400 M_{\odot}$, this paper; $7600 M_{\odot}$ from Arvidsson & Kerton (2011)) suggesting that most of the molecular material is intact by the dissociating processes.

The H I shell is thinner towards the dense molecular core, S187 NE. The shell correlates with the PDR traced at $12 \mu\text{m}$ (Fig. 18). Kirsanova & Wiebe (2019) note that a density-bounded PDR leads to the merging of the H_2 and CO dissociation fronts. In S187 NE the ^{13}CO and H I peaks are separated by less than 25 arcsec (0.2 pc) (Fig. B3), so the shock fronts are barely separated. The HCO^+ and H I emission

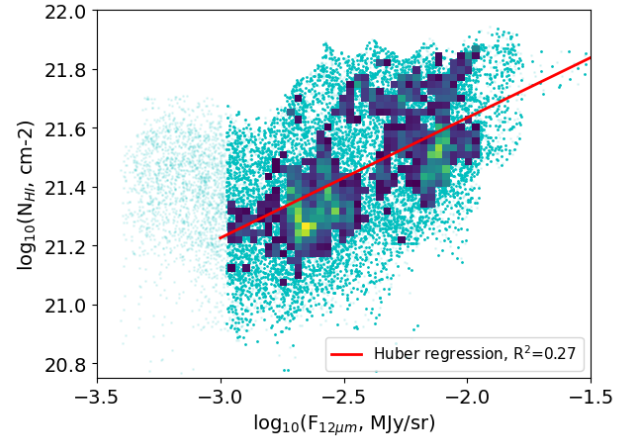


Figure 18. The correlation between the $12 \mu\text{m}$ WISE flux and H I column density.

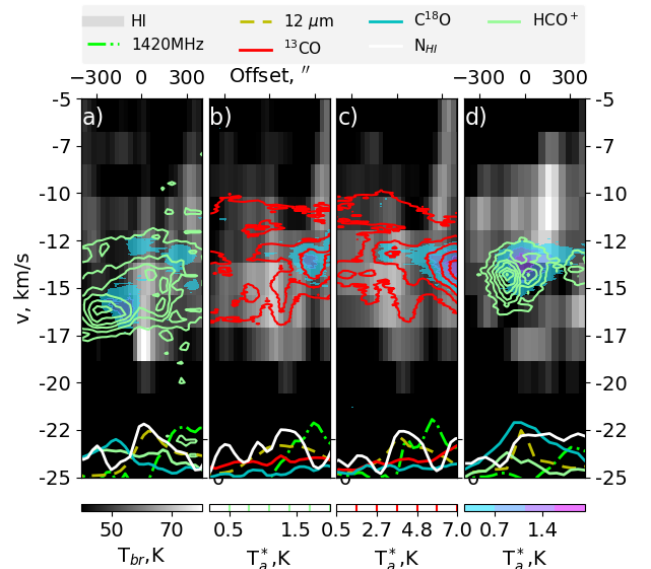


Figure 19. The position velocity diagrams across different slices of the shell (Fig. 20). a) - the slice through S187 PDR1 (positive offsets are towards S187B, the S187 exciting cluster). b) the slice along the direction where no wall is detected. c) PV slice through S187 PDR2, d) PV slice through S187 SE (S187-IRS). Normalised plots of the continuum emission and integrated ^{13}CO and C^{18}O emission along the PV slices are plotted at the bottom of the panel. (Scale factors: 8 mJy/beam, 7 GJy sr^{-1} , 17 K km s^{-1} , 2 K km s^{-1} , 6 K km s^{-1} , $5 \times 10^{21} \text{ cm}^{-2}$ for 1420 MHz continuum, $12 \mu\text{m}$ WSSA WISE, ^{13}CO , C^{18}O , HCO^+ integrated intensity and H I column density, respectively).

regions spatially and kinetically overlap (Fig. 19, a.) supposing the mixing of the fronts. The $12 \mu\text{m}$ peak may be shifted from the H I due to a projection effect as can be seen from the position-velocity diagram in Fig. 19, a., on the bottom plots. The 1420 MHz continuum is also plotted representing the ionized region. (S187 PDR1 is traced by H I and WISE $12 \mu\text{m}$ and S187 NE is traced by HCO^+ and C^{18}O). The PV cut in the direction where no PDR and molecular wall is observed is shown in Fig. 19, b. The H I emission is present,

but no compact features exist, the H I layer is broader than towards S187 PDR1, up to ~ 2.4 pc. Weak C¹⁸O and ¹³CO emissions are detected indicating a small amount of molecular material in the shell towards the location of the PV cut. The PV cut through S187 PDR2 is shown in Fig. 19, c. The C¹⁸O emission is weaker than in the S187 PDR1, but stronger than in cut b). There are WISE 12 μ m and 1420 MHz continuum peaks suggesting a compression of the gas.

5.2.1 Fragmentation

The shell has systematic motions and related kinematics, as discussed in the previous section. In addition, we observe smaller features identified as fragments in Sect. 4.1.1 and estimated their physical properties. The slope of the mass-size relation (Fig. 10) is the same as found for molecular clouds (e.g. Elmegreen & Falgarone 1996; Roman-Duval et al. 2010). Kritsuk et al. (2013) argued that supersonic turbulence fed by large-scale kinetic energy injection is at the origin of the law. The H I fragment masses are lower than masses of molecular clumps estimated by Roman-Duval et al. (2010) for the same size. This observation may result from the diffusion of the atomic gas during dissociation or transformation to the ionized gas state. The fragments may also have significant amounts of molecular material that are not completely dissociated into atomic gas. This sample can be incomplete on smaller scales where fragments can not be resolved. Such incompleteness will not affect the observed relations significantly since the detected fragment sizes vary over an order of magnitude. The peak of the fragment mass function at $\sim 1 - 3 M_{\odot}$ (Fig. 9) is very close to the peak of the prestellar core mass function in molecular clouds (e.g. Könyves et al. 2020). Most probably these fragments in the H I shell represent remnants of the molecular clumps where molecular hydrogen was dissociated by the UV radiation of the central star cluster.

The velocity dispersion in the fragments increases with the fragment size (Fig. 10) resembling one of the well-known ‘‘Larson’s laws’’ (Larson 1981). However the slope of our relation is steeper and the absolute values of the velocity dispersion are much higher than found by Larson for molecular clouds and condensations of the same size. They are also significantly higher than in massive protostellar cores (e.g. Zinchenko 2000). The mass-size relation for the optically thick limit are closer to those presented in Roman-Duval et al. (2010), especially for larger fragments. Such differences are in agreement with these fragments being the eroded material dissociating into the surroundings with higher turbulent or thermal motions than the ordinary molecular clumps. The erosion may be caused by photoevaporation (Decataldo et al. 2019). The high velocity dispersion leads to high values of the virial parameter for most fragments $\alpha \gtrsim 2$ (Figs. 9, 10), which implies that they are gravitationally unbound (e.g. Kauffmann et al. 2013). There is a trend of increasing virial parameter with fragment size. The most compact fragments are relatively dense and may represent gravitationally bound objects.

Alternatively, such fragments may form in PDR itself by dynamical compression. The shock can be caused by the external high pressure from regions heated by far ultra violet radiation. The fragments then dissociate and/or evaporate and loose mass. The timescales should be close to the estimated kinematical age of the sub-bubble (Gorti & Hollenbach 2002). During the expansion of the H II zone, the new material should be involved in the process so the variety of the physical parameters, especially densities and virial parameters should be observed. The S187 region is fairly young ($\sim 5 \times 10^5$ yr), but no radial dependence of the fragment properties is observed. It may be caused by the observational limits or projection effect. Still, the dependence of density and virial parameters on the fragment

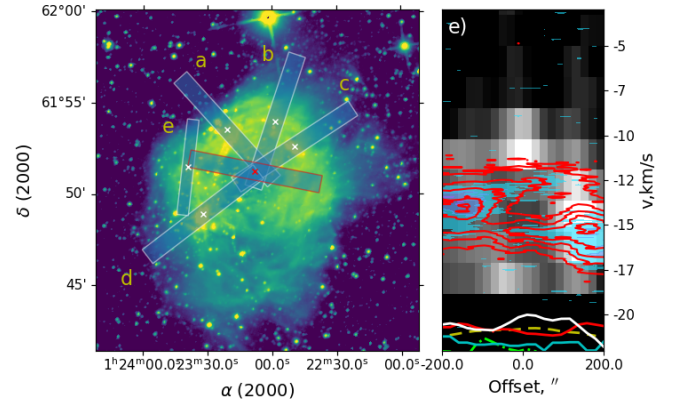


Figure 20. (Left:) Locations of the PV slices used in Fig. 19 (white boxes, with corresponding labeling) and in Fig. 16 (red box). The WISE 3.4 μ m image is in the background. (Right:) PV slice through cut e, the H I bubble. The scales, legend and colour bars are the same as in Fig. 19.

size demonstrate a larger scatter than the mass dependence on size (Fig. 10).

5.3 The stages of star formation

5.3.1 The sub-bubble

One of the most complex spatial-kinematical feature in the S187 shell is the bubble-like H I structure shown in Fig. 4 (labelled H I bubble, the coordinates are given in Table. 2). H I channel maps and PV diagram reveal the presence of the bubble-like structure that is not detected in other tracers. The spectra are shown in Fig. 5. Weak HCO⁺ and CS lines are detected. The HCO⁺ line profile resembles the ¹²CO line profile towards the sub-bubble. The C¹⁸O and CS peaks are located at -13 km s^{-1} . The position-velocity diagram is shown in Fig. 20, e). The centre of the position-velocity diagram corresponds to the Class II source position, and the slice direction is shown in Fig. 20, left. The 21-cm line emission shows the O-like PV feature tracing the expanding H I layer around the Class II object with the velocity range from -19 km s^{-1} to -8 km s^{-1} . The peak of the 12 μ m emission is close to the centre of the ‘‘O’’ ‘‘hole’’ in the H I data. The PV structure of the molecular lines is similar to the H I, but the velocity dispersion is lower than for the 21-cm line tracing outer parts of the sub-bubble. No continuum emission is detected towards the Class II object or the sub-bubble at 1.4 GHz in our data or at 8.2 and 4.9 GHz (Snell & Bally 1986). The OH maser is reported in Engels & Bunzel (2015) near the Class II source. Two molecular line components exist in the ¹³CO, C¹⁸O and HCO⁺ emission at -15 and -12.5 km s^{-1} with the approximate same structure as the atomic gas. The CS integrated emission has a weak bowed structure in the direction of the boundary of the sub-bubble, as shown in Fig. 21. The H I layer has higher intensity towards the H II region. The C¹⁸O and ¹³CO position-velocity structure correlates well with the O-shape. The bubble-like structure is shown in Fig. 20. As shown in Joncas et al. (1992) the stellar wind from the exciting cluster is pointing towards the bubble which may have triggered the early, relative to the S187 NE and SE cores, evolution. Based on the formula from Weaver et al. (1977) we estimate the age of the bubble as 6×10^4 years.

This sub-bubble structure reveals an interaction of the Class II object with ambient gas within the context of the H I shell. The location of the Class II object near the border of the ionized region suggests a triggered origin for the exciting star. A number of YSOs

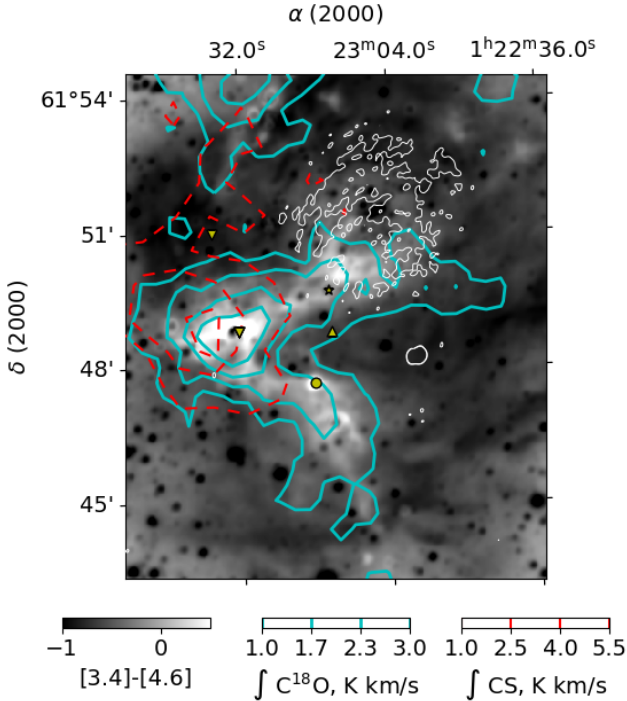


Figure 21. The molecular gas structure in $C^{18}O$ integrated emission (cyan contours), CS (2–1) integrated emission in red dashed contours and the tapered 1420 MHz continuum in white (levels: 1, 2 mJy/beam) contours over the background gray-scale image representing [3.4]–[4.6] colour. Point sources are not removed for presentation purposes. The marks are the same as in Fig. 4

are located towards the sub-bubble, especially at the boundary of S187. Some of them have X-ray emission counterparts reported in the Chandra point source 2XCO catalog (Evans et al. 2020). The excess of $12\ \mu\text{m}$ emission and the 3.4 to $4.6\ \mu\text{m}$ colour detected towards the sub-bubble (Figs. 1 and 21) imply additional production of PAHs by the exciting star and the dominance of photo dissociation near the Class-II source. The Class II source and the associated sub-bubble can lead to the additional stimulation of the YSO formation in the S187 shell environment.

5.3.2 The S187 SE core

The molecular core S187 SE is located to the south-east of the ionizing cluster S187B (Table 2). S187 SE is associated with the bright IR Class-I source IRAS 01202+6133 and maser sources. The position-velocity diagram across the core is plotted in Fig. 19, d. We define the cores as kinematically-coherent gas detected in $C^{18}O$. The internal structure of this object is quite rich. The HCO^+ , CS, HCN and N_2H^+ lines were observed by Zinchenko et al. (2009) and revealed complicated gas structure. The extended structures are similar to those observed in $C^{18}O$. Therefore, the core contains at least two dense gas fragments (probably associated with IRAS 01202+6133 and S187 H α). Ammonia emission is also detected towards S187 H α (Zavagno et al. 1994). There is a peak in the SCUBA $850\ \mu\text{m}$ image located towards S187 NIRS1 (See Fig. 1) suggesting the embeddance of this object into the S187 SE core. No associated peak in molecular lines was detected towards S187 NIRS1.

We detected compact continuum emission which possibly traces an UC H II region around IRAS 01202+6133. The H I line is less intense towards the centre position at $-15\ \text{km s}^{-1}$. The HCO^+ and $C^{18}O$ lines

have different profiles (Fig. 5) and spatial distributions (Fig. 19, d): the $C^{18}O$ emission peak is located towards IRAS 01202+6133. The HCO^+ peak at $-14.3\ \text{km s}^{-1}$ is shifted by ~ 80 arcsec from the $C^{18}O$ ($-13.6\ \text{km s}^{-1}$) peak. The $4.6/3.4\ \mu\text{m}$ ratio peak is located towards the HCO^+ peak, the CS emission peak is also shifted from IRAS 01202+6133 (Fig. 21). We interpret such differentiation as an interaction between the UC H II region and the parent molecular core. The column density traced by $C^{18}O$ associated with the core is centered at IRAS 01202+6133 where the dense part of the core is perturbed by the UC H II region. No self-absorption feature in $HCO^+(1-0)$ ($E_u \approx 4.28\text{K}$) is detected. The self-absorption was reported in $HCO^+(3-2)$ ($E_u \approx 17\text{K}$) (Kang & Kerton 2012). In case the gas is thermalized, this would be in agreement with a kinetic temperature of 9.5 K for the core.

No ^{12}CO emission peak is detected towards S187 SE. The emission can be optically thick, unlike S187 NE. The emitting region towards S187 NE is more extended than the $C^{18}O$. The ^{12}CO -traced regions, probably, represent the lower density molecular gas around the core. For S187 SE a different environment is observed: the $C^{18}O$, ^{13}CO and HCO^+ emission regions are surrounded by H I emission (see Fig. 19, d). The core is embedded into the shell. Thus, the H I gas should be produced during photo-dissociation. S187 SE is dense ($1 \times 10^5\ \text{cm}^{-3}$ Zinchenko et al. (2009)), and bright $12\ \mu\text{m}$ spots (like S187 PDR1 and S187 PDR2) should appear at the border between PDR and molecular gas, but none was detected. The molecular material traced by $C^{18}O$ is elongated to the centre of the H II region with the peak near the border of the H I layer. The orientation of the elongation seems close to the plane of the sky since no significant gradients are detected in the molecular data position-velocity diagram (Fig. 19, d). The distribution of the radio continuum emission indicates pocketing of the molecular material in the H II region too. The increasing ratio of the 160 to $12\ \mu\text{m}$ emission towards the CS and $C^{18}O$ emission region can be a tracer of the cold dust dominance over the core.

The origin of the [3.4]–[4.6] VS $C^{18}O$ correlation (Fig. 11 and 21) in S187 SE remains unknown. The presence of recombination lines (Peeters et al. 2004) can increase the $4.6\ \mu\text{m}$ flux but can only be related to the UC H II zone. The H_2 lines present in the to $4.6\ \mu\text{m}$ WISE band also can increase the colour. H_2 emission was observed by Salas et al. (1998) but shows a different morphology than the colour map. The $3.4\ \mu\text{m}$ emission can be saturated by a significant optical depth in the dense core at this wavelength (Pavlyuchenkov et al. 2012) both in PAH, silicates and grains. The optical depth at $4.6\ \mu\text{m}$ is lower so such reddening can arise. The [3.4]–[4.6] colour values is close to those presented in Ybarra et al. (2014) ([3.6]–[4.5] Spitzer) colour implying the reddening of the PDR emission in the S187 SE core.

The kinematical-morphological structure of the core and a number of active star formation processes are indicators that S187 SE has suffered from external pressure. The most obvious (and realistic) explanation is the pressure caused by H II region expansion. Still, no shock or ionisation fronts in PDRs that should be traced in $12\ \mu\text{m}$ or 3.4 to $4.6\ \mu\text{m}$ ratio are detected. The core is elongated towards the center of H II zone, and the pressure and ionizing flux can be reduced by the geometry of the core, leading to perturbation instead of dissociation. Strong dust absorption can also protect molecular material from dissociation under ionizing cluster radiation.

5.3.3 The S187 NE core

The other core (S187 NE) has a mass close to S187 SE (coordinates in Table. 2). No PDR traced by 3.6 or $4.6\ \mu\text{m}$ emission peaks observed

under the $C^{18}O$ contours suggesting that the core is mostly intact from the expansion of the $H\ II$ region. The PDR is located between the $H\ II$ zone and the molecular gas, as shown in Fig. 4 (S187 PDR1). The structure of the PDR, $H\ I$ and molecular layers are shown in a PV (Fig. 19, a) plot. The transition between the unperturbed and the affected by $H\ II$ zone material is seen, with the HCO^+ line broadening overlapping with the $H\ I$ emission. Class-I and Class-II sources are located between the S187 NE core and S187 $H\ II$ region, but no IR sources are detected in S187 NE according to the WISE images.

The molecular spectra of S187 NE are shown in Fig. 5. Unlike the other cores and PDRs, the HCO^+ and ^{12}CO line profiles are close to the $C^{18}O$ ones, at $-16.4\ km\ s^{-1}$. No CS peak is observed within A 1 K sensitivity. The CS(2–1) and $HCO^+(1-0)$ transitions upper energies are close (7.1 and 4.28 K, respectively (Shirley 2015)). The critical density of the CS(2–1) transition ($1.3 \times 10^5\ cm^{-3}$) is two times higher than for $HCO^+(1-0)$ ($6.8 \times 10^4\ cm^{-3}$) (Shirley 2015). The absence of CS may indicate A low density for this core or chemical processes varying the abundance.

The PV cut in Fig. 19, a indicates an increase of the FWHM of the $C^{18}O$ line from 1.4 to $3.6\ km\ s^{-1}$ towards the ionized region. This effect can trace the turbulent motions caused by the expansion of the S187 shell. This effect by similar effects as for $H\ I$ fragments (See Sect.5.2.1). The profile is far from Gaussian, as shown in Fig. 5. The HCO^+ line emission (Fig. 19, a) has two components. One is a compact narrow peak shifted by ~ 60 arcsec from the $C^{18}O$ peak outwards of S187 B. The wider ($\sim 5\ km\ s^{-1}$) weak emission correlates with the $H\ I$ emission and is shifted towards S187 B by ~ 80 arcsec. We associate this component with the photo-dissociation processes, consistent with modelling (Kirsanova et al. 2020).

The ^{12}CO peak is shifted by 40 arcsec from the $C^{18}O$ peak to the centre of the $H\ II$ region (Fig. B1). Since the ^{12}CO emission can trace the kinetic temperature (Wilson et al. 2012) this effect may be explained by heating of the core by the PDR. The PDR is brighter towards the core indicating feedback from the core to the shell. Another possibility is an optical depth effect, which should be greater towards the center of the core. The free-free continuum is also intense in this direction simultaneously with the peaks in the $H\ I$ line. The blue spot in Fig. 12 is located just between the cold dust layer (green) and the PDR (red). This spot is well-correlated with the atomic gas emission in the 21-cm line and the HCO^+ extended feature. This excess could be related to the shocked gas excited in $Br\alpha\ 4.06\ \mu m$ line, as observed in Orion Bar (Verstraete et al. 2001). This region was observed in the H_2 line (Salas et al. 1998) and no associated peak was reported. We also note that no extended green object is reported in S187 NE.

Some $C^{18}O$ emission peaks were also detected in the northern and western part of the shell, as seen in Fig. B2. The coordinates are $\alpha=1^h 22^m 59^s.3$, $\delta=+61^\circ 42' 28''.8$ and $1^h 22^m 41^s.1$, $+61^\circ 49' 54''.3$. They are not covered by CS and HCO^+ observations and are not discussed in this paper.

5.4 The PDRs

Our observations trace the structures of dissociation regions under different physical conditions. The structures are represented in the position-velocity diagrams (Fig. 19) and in maps (Fig 4, left). The general structure is close to that presented in Tielens & Hollenbach (1985); Gorti & Hollenbach (2002). The close-up map of the S187 PDR1 and S187 PDR2 is shown in Fig 4, b) and c).

We observe free-free continuum, $12\ \mu m$, $H\ I$ CO, HCO^+ and $C^{18}O$ emission peaks sequentially from the S187B exciting cluster to the S187 NE core in S187 PDR1. The spatial-kinematic structure sug-

gests an edge-on configuration of the PDR (Fig. 4, c), Fig. 19, a)). The HCO^+ line is observed in the molecular core and towards the wall traced by the $H\ I$ line, as shown in Fig 19, a, in the center of the picture. The line width increases towards the S187 PDR1. The line profile is far from Gaussian and has multiple peaks (Fig. 5). No absorption profile is observed towards the molecular core S187 NE (unlike for S187 SE, (Kang & Kerton 2012)) implying the same towards S187 PDR1. No $C^{18}O$ or SCUBA $850\ \mu m$ emission is detected towards the HCO^+ peak in S187 PDR1. The line centroid velocity is $\sim 15\ km/s$.

The HCO^+ emitting gas is probably located behind the shocks ($5.8\ \mu m$ Spitzer) and the atomic gas shell layer (See Fig. 4, c.). This picture does not match the classical (Sternberg & Dalgarno 1995) view of the evolution of PDR region, where atomic gas is located between $H\ II$ and the molecular material. The structures observed at $5.8\ \mu m$ look filamentary, unlike in S187 PDR2. A Class-II source is detected towards the S187 PDR1 HCO^+ line peak. The gas associated with that peak may survive after the shock passage. The HCO^+ abundance should increase under this process. But, there is no direct evidence of such scheme and A high-resolution multi-line analysis is necessary to study the state of the molecular gas in S187-PDR1. The difference between HCO^+ and H_2 dissociation fronts is modeled in Kirsanova & Wiebe (2019). Such difference may be increased by fragmentation of the gas. The PV diagram of the $H\ I$ line is not symmetric relative TO the molecular line peaks. Molecular lines are brighter at the positive velocities. The $H\ I$ line peak is slightly shifted to negative velocity. Since the atomic gas is generated during dissociation, the effect may be caused by non-uniform irradiation or weakening by the HCO^+ traced gas fragment.

According to PV diagrams (Fig. 19, c)), the S187 PDR2 region is more or less edge-on with respect to the observer ($\sim 20^\circ$). A weak $C^{18}O$ emission region associated with SCUBA $850\ \mu m$ peak is located at $-12\ km/s$ (Fig. 19, c, Fig. 4, b. and Fig. 1) near S187 PDR2. Structure of the $5.8\ \mu m$ Spitzer and the $4.6\ \mu m$ WISE emission suggest shielding by molecular material. The column density map (Fig. 7) shows that the atomic gas is concentrated near the $H\ II$ zone border. The $H\ I$ PV diagram indicate presence of the border towards the $H\ II$ zone, same as for (Fig 19, b) where no shielding by molecular material is observed. The PV diagram (Fig. 19, b) and channel maps (Fig. B1,B2,B3) trace leaking $H\ II$ zone emission trailing up to 4 pc from the center of the $H\ II$ zone. From the spatial-kinematic structure of the $H\ I$ emission we conclude that the $H\ II$ zone is not effectively shielded by molecular gas or dust fractions.

6 CONCLUSION

We studied the shell around the S187 $H\ II$ region in the $H\ I$ 21 cm line, molecular lines, and also in infrared and radio continua. The region is mostly circular, but the emission is not homogeneous. The 1420 MHz continuum emission peaks are correlated with the PDR traced by WISE and Spitzer data. We detected an excess of $H\ I$ emission towards the $H\ II$ region tracing the shell. It has a shape close to circular, the peaks correlate with PDRs. The position-velocity diagram in the $H\ I$ line has the O-type shape typical of an expanding atomic layer in this case at the boundary of the $H\ II$ region. The shell has a molecular component visible in the ^{12}CO (1–0) line. The $C^{18}O$ (1–0) and $H\ I$ emission distribution are spatially and kinematically related. The molecular part of the shell is more extended than the atomic one. The expansion speed is $\sim 7.5\ km\ s^{-1}$. The sandwich-like composition of the ionized-PDR-HI-molecular gas structure of the $H\ II$ region and its environment is defined by different tracers.

Summary:

(i) We present the results of high-resolution 8 arcsec (0.06 pc) observations of the H I line emission towards the S187 H II region. To our knowledge, this is the highest resolution available of the H I emission observations of Galactic regions.

(ii) We resolved the NVSS 012258+614815 source as two separate sources with individual H I absorption profiles. By combining with the emission spectra we estimated optical depth profiles. The mass of the atomic gas related to S187 is estimated as $260 \pm 56 M_{\odot}$ using the emission and absorption data. The median spin temperature over the shell is ~ 50 K. The size of the shell is ~ 4 pc. The H I layer has varying thickness from 0.2 pc to 4 pc.

(iii) The distribution of the neutral atomic gas is close to an expanding sphere, spatially correlating with the WISE 12 μ m emission and traces the interaction between the H II region and the molecular cloud.

(iv) The atomic shell is inhomogeneous and contains ~ 100 fragments of median mass around $\sim 1.1 M_{\odot}$. The total mass estimation is in $114\text{--}240 M_{\odot}$ (depending on optical depth assumption) which is close to the overall shell mass. The fragment sizes vary from 0.03 to 0.23 pc and the index of the mass-size power-law fit is 2.33–2.6 range. This estimation is close to previously reported values available in the literature for molecular gas clumps and clouds. These fragments can be the dissociating molecular prestellar cores under UV erosion. Alternatively, such fragments may be formed in the PDR by impulse heating and turbulent motions.

(v) We detect an H I sub-bubble inside the H I shell. A group of young stellar objects is detected in the direction of the walls, their formation may be induced by the interaction between the bubble and the shell. The sub-bubble is young with a kinematical age of $\sim 10^5$ years.

(vi) Two molecular cores (NE and SE) are present in the S187 environment. They have similar masses ($\sim 1200 M_{\odot}$ and $\sim 900 M_{\odot}$, respectively) and different physical conditions. S187 SE contains a number of young stellar objects, an IRAS source, outflows and a number of other signs of ongoing star formation, which is an argument of a past interaction with the H II zone. The spatial-kinematic relation between the H I and ^{12}CO emission implies ongoing interaction between the atomic shell and the molecular core, but no shock signatures or PDR AT the border are observed. The S187 SE virial parameter is ~ 2.75 . S187 NE is being compressed by the shell and its virial parameter is ~ 1.4 . No significant star formation activity is detected inside the core. Three YSOs are present inside the H I shell contact zone. The distribution of molecular lines suggests heating and the increase of turbulence near the contact zone. The core periphery located towards the H I shell and the H II zone is eroded by the radiation field.

(vii) The WISE [3.4]–[4.6] colour correlates with the column density of the molecular gas. One of the most reasonable explanation is the effect of photon absorption by grains in the dense molecular gas of S187 SE.

(viii) The H I line radial plots and position-velocity diagrams are different for the directions where the H II region is bounded by dense gas and where it is not. The PV diagram has an O-type shape where the shell is density bounded. In the regions where no dense structures are detected, the PV structures are irregular.

ACKNOWLEDGEMENTS

We are thankful to Maria Murga, Yaroslav Pavlyuchenkov and Maria Kirsanova for helpful discussions and consultations. We appreciate

by Kim Ardvisson and Cris Ardvisson for providing CO isotopologues observations data. We thank the anonymous reviewer for a critical reading of the manuscript and the useful and thoughtful comments and suggestions, which greatly improved the contents of the paper.

This work was supported by the Russian Science Foundation under project No. 17-12-01256 (the H I line, molecular observations and analysis, physical parameter estimations). The dust emission analysis was supported by the Foundation for the Advancement of Theoretical Physics and Mathematics “BASIS”.

The Canadian Galactic Plane Survey (CGPS) is a Canadian project with international partners. The Dominion Radio Astrophysical Observatory is operated as a national facility by the National Research Council of Canada. The Five College Radio Astronomy Observatory CO Survey of the Outer Galaxy was supported by NSF grant AST 94-20159. The CGPS is supported by a grant from the Natural Sciences and Engineering Research Council of Canada.”

We acknowledge support from the Onsala Space Observatory for the provisioning of its facilities/observational support for obtaining the HCO⁺ data. The Onsala Space Observatory national research infrastructure is funded through Swedish Research Council grant No 2017-00648.

We thank the staff of the GMRT who have made these observations possible. DKO and SKG acknowledge the support of the Department of Atomic Energy, Government of India, under project Identification No. RTI 4002.

DATA AVAILABILITY

The raw data underlying this article are available in the GMRT Online Archive at <https://naps.ncra.tifr.res.in/goa/data/search>, and can be accessed with Project Code 26_012.

The processed data underlying this article (combined GMRT and CGPS datacube) are available in Zenodo, at [doi:10.5281/zenodo.5070398](https://doi.org/10.5281/zenodo.5070398)

REFERENCES

- Aniano G., Draine B. T., Gordon K. D., Sandstrom K., 2011, *PASP*, **123**, 1218
- Arvidsson K., Kerton C. R., 2011, *AJ*, **141**, 153
- Astropy Collaboration et al., 2013, *A&A*, **558**, A33
- Bally J., Chambers E., Guzman V., Keto E., Mookerjee B., Sandell G., Stanke T., Zinnecker H., 2018, *AJ*, **155**, 80
- Belitsky V., et al., 2015, *A&A*, **580**, A29
- Berry D. S., 2015, *Astronomy and Computing*, **10**, 22
- Burton W. B., 1971, *A&A*, **10**, 76
- Cichowolski S., Romero G. A., Ortega M. E., Cappa C. E., Vasquez J., 2009, *MNRAS*, **394**, 900
- Cichowolski S., Pineault S., Gamen R., Arnal E. M., Suad L. A., Ortega M. E., 2014, *MNRAS*, **438**, 1089
- Cutri R. M., et al., 2003, 2MASS All Sky Catalog of point sources.
- Decataldo D., Pallottini A., Ferrara A., Vallini L., Gallerani S., 2019, *MNRAS*, **487**, 3377
- Draine B. T., Li A., 2007, *ApJ*, **657**, 810
- Elmegreen B. G., Falgarone E., 1996, *ApJ*, **471**, 816
- Engels D., Bunzel F., 2015, *A&A*, **582**, A68
- Evans I. N., et al., 2020, in American Astronomical Society Meeting Abstracts #235. p. 154.05
- Fontani F., Giannetti A., Beltrán M. T., Dodson R., Rioja M., Brand J., Caselli P., Cesaroni R., 2012, *MNRAS*, **423**, 2342
- Gorti U., Hollenbach D., 2002, *ApJ*, **573**, 215

- Han F., et al., 1995, Publications of the Purple Mountain Observatory, **14**, 185
- Henkel C., Haschick A. D., Guesten R., 1986, *A&A*, **165**, 197
- Israel F. P., 1977, *A&A*, **61**, 377
- Jackson J. M., et al., 2006, *ApJS*, **163**, 145
- Joncas G., Durand D., Roger R. S., 1992, *ApJ*, **387**, 591
- Kang S.-J., Kerton C. R., 2012, *ApJ*, **759**, 13
- Kang S.-J., Kerton C. R., Choi M., Kang M., 2017, *ApJ*, **845**, 21
- Kauffmann J., Pillai T., Goldsmith P. F., 2013, *ApJ*, **779**, 185
- Kirsanova M. S., Wiebe D. S., 2019, *MNRAS*, **486**, 2525
- Kirsanova M. S., et al., 2020, *MNRAS*, **497**, 2651
- Koenig X. P., Leisawitz D. T., 2014, *ApJ*, **791**, 131
- Könyves V., et al., 2020, *A&A*, **635**, A34
- Kritsuk A. G., Lee C. T., Norman M. L., 2013, *MNRAS*, **436**, 3247
- Larson R. B., 1981, *MNRAS*, **194**, 809
- Leahy D., Tian W., 2006, *A&A*, **451**, 251
- Mangum J. G., Shirley Y. L., 2015, *PASP*, **127**, 266
- McMullin J. P., Waters B., Schiebel D., Young W., Golap K., 2007, in Shaw R. A., Hill F., Bell D. J., eds, *Astronomical Society of the Pacific Conference Series Vol. 376, Astronomical Data Analysis Software and Systems XVI*. p. 127
- Meisner A. M., Finkbeiner D. P., 2014, *ApJ*, **781**, 5
- Meisner A. M., Lang D., Schlegel D. J., 2017, *AJ*, **154**, 161
- Newville M., Stensitzki T., Allen D. B., Ingargiola A., 2014, *LMFIT: Non-Linear Least-Square Minimization and Curve-Fitting for Python*, doi:10.5281/zenodo.11813, <https://doi.org/10.5281/zenodo.11813>
- Nguyen H., Dawson J. R., Lee M.-Y., Murray C. E., Stanimirović S., Heiles C., Miville-Deschênes M. A., Petzler A., 2019, *ApJ*, **880**, 141
- Okada Y., Güsten R., Requena-Torres M. A., Röllig M., Stutzki J., Graf U. U., Hughes A., 2019, *A&A*, **621**, A62
- Palagi F., Cesaroni R., Comoretto G., Felli M., Natale V., 1993, *A&AS*, **101**, 153
- Pavlyuchenkov Y. N., Wiebe D. S., Akimkin V. V., Khramtsova M. S., Henning T., 2012, *MNRAS*, **421**, 2430
- Pedregosa F., et al., 2011, *Journal of Machine Learning Research*, **12**, 2825
- Peters E., Allamandola L. J., Bauschlicher C. W. J., Hudgins D. M., Sandford S. A., Tielens A. G. G. M., 2004, *ApJ*, **604**, 252
- Pineda J. L., Langer W. D., Velusamy T., Goldsmith P. F., 2013, *A&A*, **554**, A103
- Pirogov L. E., Zemlyanukha P. M., 2021, *Astronomy Reports*, **65**, 82
- Rau U., Naik N., Braun T., 2019, *AJ*, **158**, 3
- Reach W. T., Heiles C., 2021, *ApJ*, **909**, 71
- Reach W. T., Bernard J.-P., Jarrett T. H., Heiles C., 2017, *ApJ*, **851**, 119
- Requena-Torres M. A., Israel F. P., Okada Y., Güsten R., Stutzki J., Risacher C., Simon R., Zinnecker H., 2016, *A&A*, **589**, A28
- Richards E. E., Lang C. C., Trombley C., Figer D. F., 2012, *AJ*, **144**, 89
- Roger R. S., McCutcheon W. H., Purton C. R., Dewdney P. E., 2004, *A&A*, **425**, 553
- Roman-Duval J., Jackson J. M., Heyer M., Rathborne J., Simon R., 2010, *ApJ*, **723**, 492
- Russeil D., Adami C., Georgelin Y. M., 2007, *A&A*, **470**, 161
- Saha P., Roy N., Bhattacharya M., 2018, *MNRAS*, **480**, L126
- Salas L., Cruz-González I., Porras A., 1998, *ApJ*, **500**, 853
- Shirley Y. L., 2015, *PASP*, **127**, 299
- Slysh V. I., Valts I. E., Kalenskii S. V., Voronkov M. A., Palagi F., Tofani G., Catarzi M., 1999, *A&AS*, **134**, 115
- Snell R. L., Bally J., 1986, *ApJ*, **303**, 683
- Speagle J. S., 2019, arXiv e-prints, p. arXiv:1909.12313
- Sternberg A., Dalgarno A., 1995, *ApJS*, **99**, 565
- Sternberg A., Le Petit F., Roueff E., Le Bourlot J., 2014, *ApJ*, **790**, 10
- Sunada K., Nakazato T., Ikeda N., Hongo S., Kitamura Y., Yang J., 2007, *PASJ*, **59**, 1185
- Taylor A. R., et al., 2003, *AJ*, **125**, 3145
- Thompson M. A., White G. J., Morgan L. K., Miao J., Fridlund C. V. M., Huldgren-White M., 2004, *A&A*, **414**, 1017
- Tielens A. G. G. M., Hollenbach D., 1985, *ApJ*, **291**, 722
- Tody D., 1986, in Crawford D. L., ed., *Society of Photo-Optical Instrumentation Engineers (SPIE) Conference Series Vol. 627, Instrumentation in astronomy VI*. p. 733, doi:10.1117/12.968154
- Topchieva A., Wiebe D., Kirsanova M., Krushinsky V., 2017, in Balega Y. Y., Kudryavtsev D. O., Romanyuk I. I., Yakunin I. A., eds, *Astronomical Society of the Pacific Conference Series Vol. 510, Stars: From Collapse to Collapse*. p. 98
- Valdettaro R., et al., 2001, *A&A*, **368**, 845
- Verstraete L., et al., 2001, *A&A*, **372**, 981
- Weaver R., McCray R., Castor J., Shapiro P., Moore R., 1977, *ApJ*, **218**, 377
- Wilson T. L., Rohlf K., Huttemeister S., 2012, *Tools of Radio Astronomy*, 5th edition
- Wright E. L., et al., 2010, *AJ*, **140**, 1868
- Yamamura I., Makiuti S., Ikeda N., Fukuda Y., Oyabu S., Koga T., White G. J., 2010, *VizieR Online Data Catalog*, p. II/298
- Yan Q.-Z., Yang J., Sun Y., Su Y., Xu Y., Wang H., Zhou X., Wang C., 2021, *A&A*, **645**, A129
- Ybarra J. E., Tapia M., Román-Zúñiga C. G., Lada E. A., 2014, *ApJ*, **794**, L25
- Zavagno A., Deharveng L., Caplan J., 1994, in The P. S., Perez M. R., van den Heuvel E. P. J., eds, *Astronomical Society of the Pacific Conference Series Vol. 62, The Nature and Evolutionary Status of Herbig Ae/Be Stars*. p. 347
- Zinchenko I. I., 2000, *Astronomy Letters*, **26**, 802
- Zinchenko I., Pirogov L., Toriseva M., 1998, *A&AS*, **133**, 337
- Zinchenko I., Caselli P., Pirogov L., 2009, *MNRAS*, **395**, 2234

APPENDIX A: K-NEAREST NEIGHBOR REGRESSION FOR H I MAPS FITTING

This appendix describes the usage of the k-Nearest Neighbors regression for the analysis of the spectral maps using the Gaussian or simple radiative transfer models. The common way is to perform individual point-by-point least squares fitting of the model parameters. The major problem of this approach is that the results of the fitting are heavily dependent on the initial conditions of the fitting procedure. The H I spectra can consist of a number of peaks represented by individual Gaussians which lead to cases where no single statistically important solution exists. This effect increases with decreasing signal-to-noise ratio. The model parameters and its confidence regions can be found using the sampling of the likelihood function by Monte Carlo Markov Chains (Speagle 2019), by grid sampling of dimensionally-reduced space (Pirogov & Zemlyanukha 2021) or other similar sampling methods. Such approach is problematic for spectral map analysis OF individual positions. The computational complexity of sampling is quite high (especially for high dimension models) which should be repeated for individual positions and likelihood functions.

In the case of S187 H I data there is a position on the map where the parameters are known by analysis of the absorption spectra. Such information can be used for the map analysis. We assume that the physical parameters are spatially-correlated, and the results of the previous fittings can be used as the initial parameters for gradient descent (or similar) methods. We define the residual:

$$\chi^2 = \frac{1}{N_v - N_p} \sum_{i=1}^{N_v} \frac{(I_i^{obs} - I_i^{mod})^2}{\sigma^2}, \quad (A1)$$

where N_p is the number of parameters in the model, N_v is the number of spectral channels used for fitting. I_i^{obs} is the observed intensity of the spectral channel i and I_i^{mod} is the model intensity (from the Eq. 2). We use LMFIT (Newville et al. 2014) procedure and Levenberg–Marquardt algorithm to find the minimum of the residual

function. In general, the initial conditions for the fitting procedure can be approximated from previous calculations in different positions of the map. We use the k-Nearest Neighbor (kNN) regression as the approximation:

$$p_k = \frac{\sum_{j=1}^m p_j d(I_k, I_j)^2}{\sum_{j=1}^m d(I_k, I_j)^2}, \quad (\text{A2})$$

where p_k is the model parameter value, $d(I_1, I_2)$ is the distance between two spectra defined as:

$$d(I_1, I_2) = \sqrt{N_v^{-1} \sigma_1 \sigma_2 \times \sum_{j=1}^{N_v} (I_{1j} - I_{2j})^2}, \quad (\text{A3})$$

where m is the number of Nearest Neighbors used for the estimation. We use the Euclidean metric in neighbors space. This is equal to a weighted average of the model parameters from k samples. These k samples are chosen by minimal squared deviation from current spectra. We normalize the distance by the number of spectral channels and the RMS deviation estimated in line-free channels. The effect of the number of channels is not important since it is the same for the map. The distance to noisier data is increased by multiplying BY σ . We use the procedures from SCIKIT-LEARN (Pedregosa et al. 2011) in our algorithm. Using this approach we reduce the initial conditions problem to the adequate sample generation. The absorption spectra decomposition results and the Least Squares fitting results was used to fill the samples. We repeat map analysis a number of times until the results converge. The algorithm used to estimate the physical parameters of the map follows this sequence:

- (i) Estimate the optical depth and spin temperature profile from the absorption and emission spectra.
- (ii) Fit the profile with the flat-layer model.
- (iii) Fit the emission spectra to the nearest positions with the initial conditions from the previous step. Mark the positions as fitted and put the observed spectra and the fitted results in the dataset.
- (iv) Fit the nearest unfitted positions with the initial conditions estimated using kNN and the dataset. Mark the positions as fitted.
- (v) Repeat the previous step until the full map is fitted.
- (vi) Repeat the previous two steps starting from positions near the absorption: refit every position with new initial conditions from kNN results. Repeat until the fitted results for individual positions converge.

The aim of such iterations is to fill the training set for kNN regression. We repeat the whole map analysis until the initial conditions estimated by kNN for the least-squares fitting will be close to the fitted results. The initial conditions obtained by averaging the results from the similar spectra also reduce the computation cost. The insufficient sampling of the training set on the first iteration is negated by the next iterations. Such an approach is relatively computationally efficient because the initial conditions are close to the fitted results and the gradient descent (or similar) methods need a large number of iterations to fall into a residual minima. The only assumption is that the same physical properties produce the same spectra. Still, the interval of the confident estimation in individual fit is important and can be used for the analysis of the regions where the estimation is reasonable and where it is not.

APPENDIX B: FIGURES

This paper has been typeset from a $\text{\TeX}/\text{\LaTeX}$ file prepared by the author.

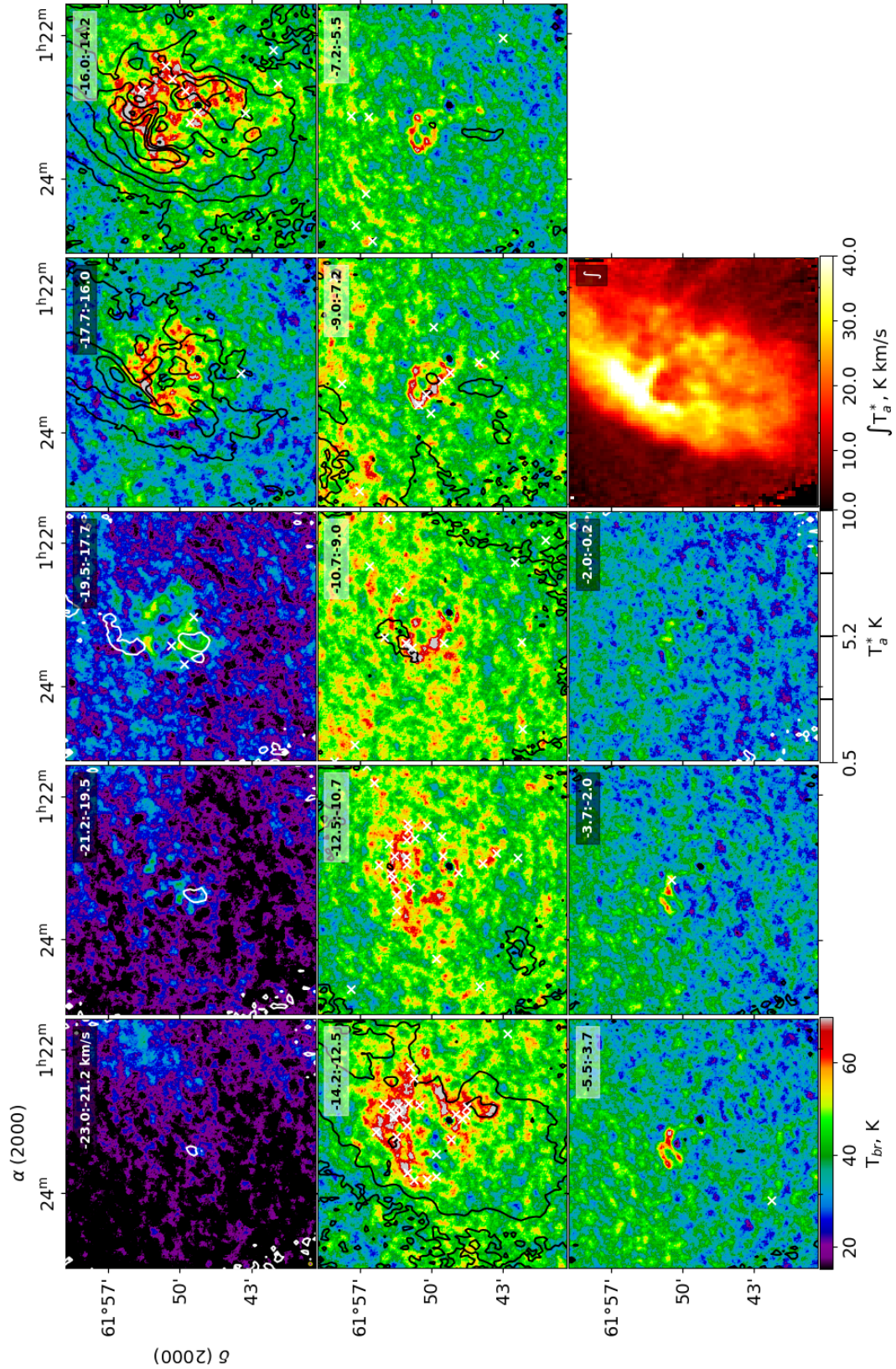


Figure B1. The channel maps of the S187 environment. The ^{12}CO (1-0) emission is in black contours. The combined GMRT+CGPS H I channel maps are shown in the background image. The beams are shown in lower-left corner of the first subplot. The velocity ranges are labeled at the top-right of every subplot. The integrated ^{12}CO (1-0) line emission is shown in the last subplot. The fragments identified by Fellwalker algorithm (See sect. 4.1.1) is shown as white crosses.

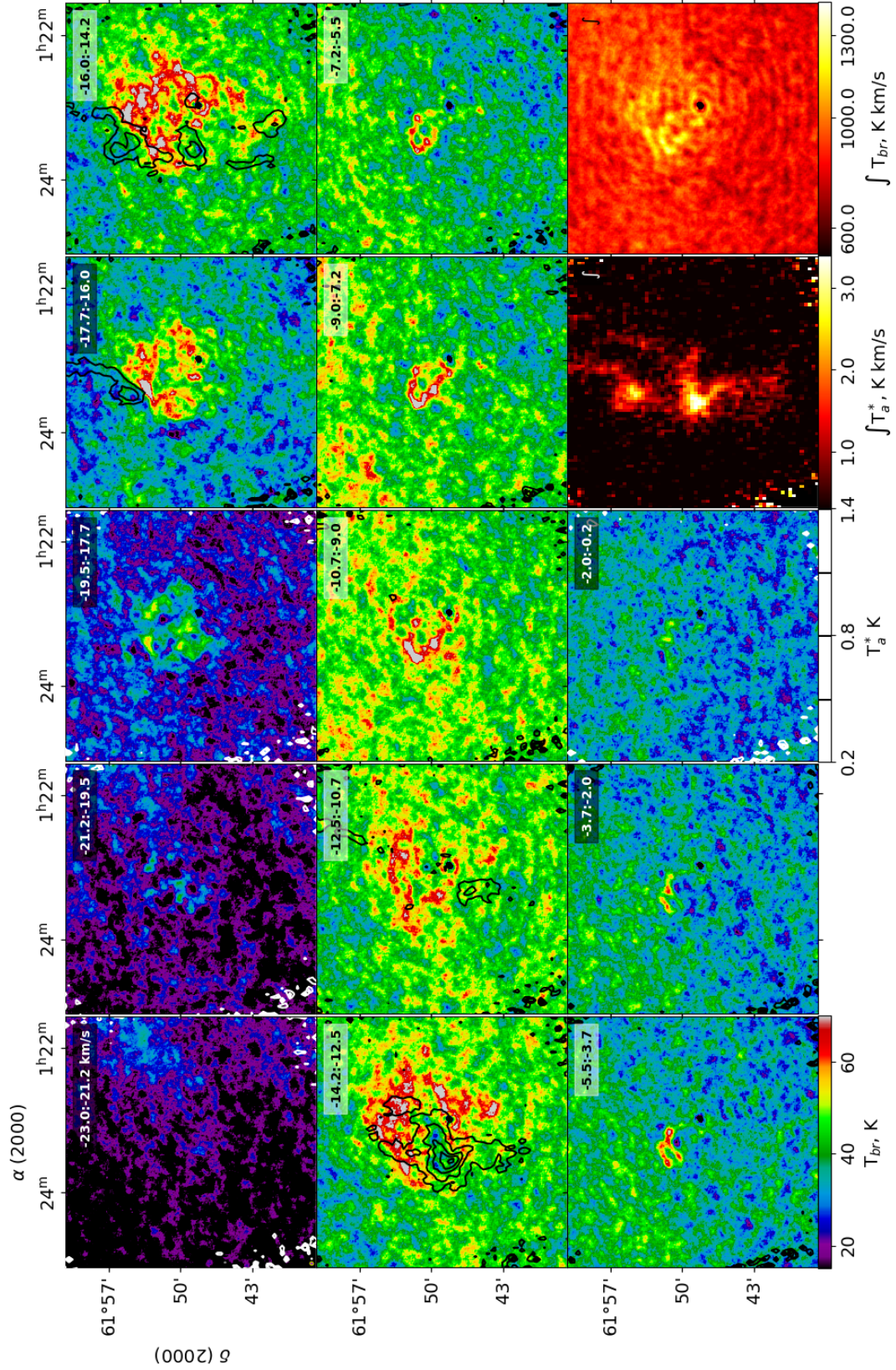


Figure B2. The channel maps of the S187 environment. The C^{18}O (1-0) emission is in black contours. The combined GMRT+CGPS H I channel maps are shown in the background image. The beams are shown in lower-left corner of the first subplot. The velocity ranges are labelled at the top-right of every subplot. The penultimate last subplot represents integrated emission of C^{18}O (1-0) and the 21-cm line integrated emission image is shown in the last subplot.

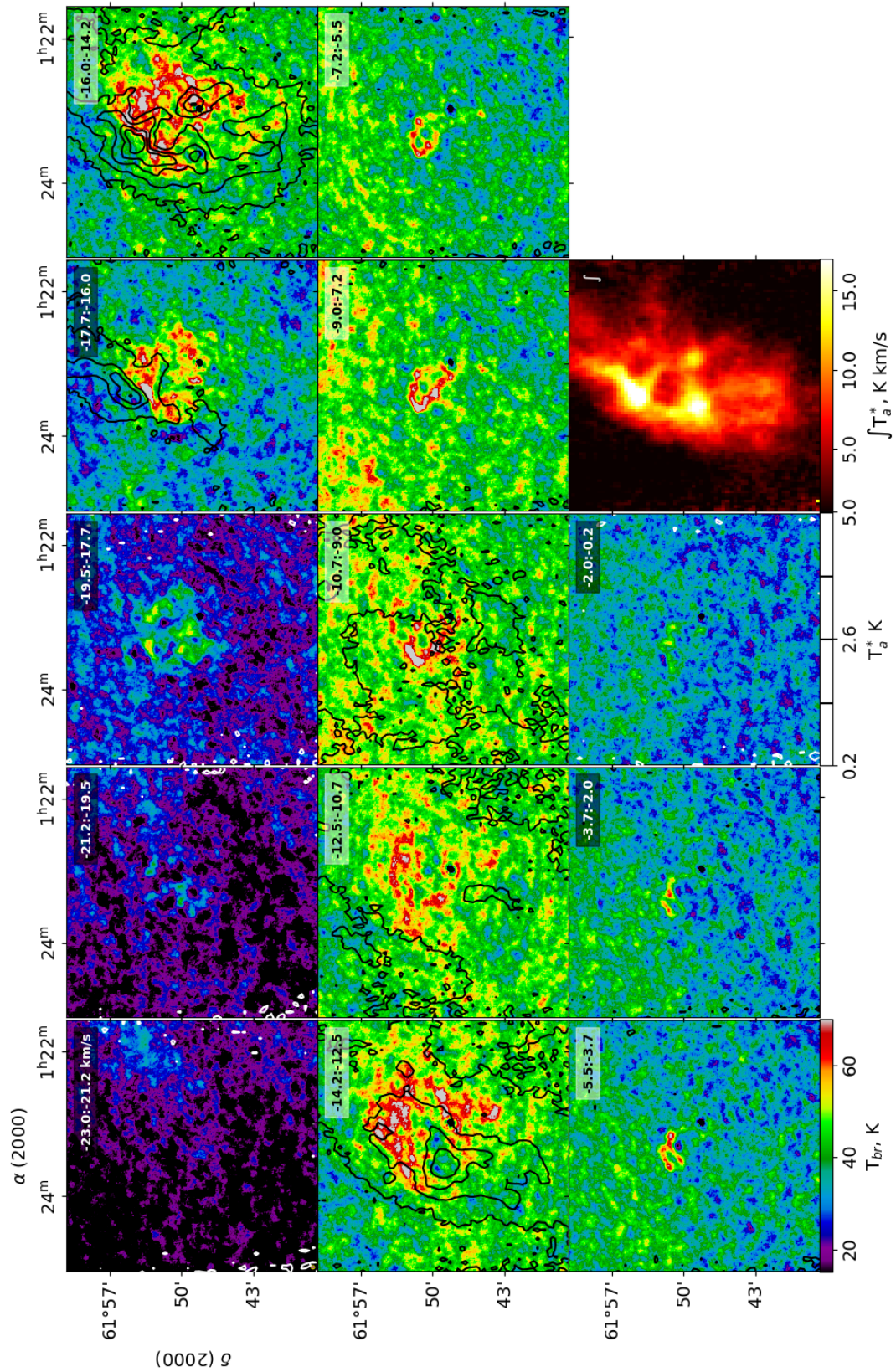


Figure B3. Same as for Fig. B1, but for $^{13}\text{CO} (1-0)$